Universitetet i Stavanger

FACULTY OF SCIENCE AND TECHNOLOGY

MASTER'S THESIS

Study programme/specialisation: **Petroleum Technology/Well Engineering**	Spring semester, 2017 **Open**
Author: **Reinert Stokkeland**	…… (signature of author)
Programme coordinator: **Professor Rune Wiggo Time** Supervisor: **Milad Khatibi**	
Title of master's thesis: **Using differential pressure and image processing for cuttings transportation measurements**	
Credits: 30	
Keywords: Cuttings transportation Particle dunes Differential pressure Fast Fourier Transform Image processing	Number of pages: 60 + supplemental material/other: 3 Stavanger, 15.06.2017

Using differential pressure and image processing for cuttings transportation measurements

Reinert Stokkeland

University of Stavanger

June 2017

Preface

First, I would like to thank professor Rune W. Time for the opportunity to write the thesis on an extremely interesting topic. His advice and pushes in the right direction has been really appreciated.

Next, I would like to thank Milad Khatibi for his extraordinary effort to help me and my fellow students. The assistance, advice, and numerous discussions throughout the writing of this thesis has been immensely helpful and I am forever grateful.

Also, Hermonja A. Rabenjafimanantsoa also deserves appreciation and thanks for the unrestricted access given to the lab.

Finally, I would like to express my gratitude towards my friends and family, for the patience displayed during this period.

Abstract

Dynamic aspects of liquid-particle flow were investigated through frequency analysis of pressure gradients and image processing of particle flow patterns. Experiments were conducted in a medium-scale flow loop with a horizontal and an inclined test section. The inclined section contained a drill string, capable of rotating, to simulate annular flow. Experiments were run on single-phase liquid and two-phase liquid-particle flow. The liquid used in the experiments was water and the particles were glass pellets. The pressure gradients for both test sections were recorded at different superficial liquid velocities for both single and two-phase flows. In addition to the pressure gradient, images of the liquid-particle flow were recorded, using high-speed cameras. The pressure gradients were converted from the time domain into the frequency domain, by applying Fast Fourier Transform on the time series of the data. An algorithm was developed to post-process the images and was written as a graphical user interface (GUI) in Matlab. The GUI was able to calculate the dune front velocity, the particle concentration in the static and moving layer as well as the changes in the bed height. The GUI was only applicable to the horizontal section, as the drill string in the inclined section caused problems with the processing. The dune front velocity calculated from a cross-correlation of the images matched up well with the amplitude peaks in the frequency spectrum.

Content

List of Figures

Nomenclature

A_{ml}	Cross-sectional area of the moving layer
A_{sl}	Cross-sectional area of the static layer
$C_{p,ml}$	Particle concentration of the moving layer in the recorded section
$C_{p,sl}$	Particle concentration of the static layer in the recorded section
DFT	Discrete Fourier Transform
dP/dL	Pressure gradient [Pam^{-1}]
DS	Drill String
FFT	Fast Fourier Transform
FPS	Frames per second
GUI	Graphical User Interface
HTS	Horizontal Test Section
ID	Inner Diameter
ITS	Inclined Test Section
LED	Light-Emitting Diode
OD	Outer Diameter
PSD	Power Spectral Density
RPM	Rotations Per Minute
u,u_p	Horizontal velocity of the particle dune front
U_{sl}	Superficial velocity of liquid in pipe flow [ms^{-1}]
$U_{sl,a}$	Superficial velocity of liquid in annular flow [ms^{-1}]
V_{pipe}	Volume of the pipe in the recorded section
ω	RPM of the Drill String

1 Introduction

1.1 Motivation

Two-phase liquid-particle flow is of importance in many modern industries, ranging from the food industry to the coal industry. Liquid-particle flow in the drilling industry is of particular interest for this thesis. The hydraulic transportation of cuttings is a complex topic, where many details remain to be understood. With further reaching and more advanced well paths the challenges imposed by cuttings transportation become increasingly relevant. Research has shown that a bed of cuttings form for low flow velocities (Tomren, Iyoho & Azar, 1986). The severity of the formation of beds increases with an increase of the angle from vertical, with the most critical angles being 40-50°, where particles will start to slide down the bore hole to form beds. Further developing the understanding of the liquid-particle flow is essential to reach the objective, to reduce down-time, and to increase profit margins.

1.2 Aim of the Study

The purpose of this study is to investigate the periodic behaviour of the pressure gradient for single-phase liquid and two-phase liquid-particle flows in a pipe and also in an annulus. The liquid for the single and two-phase flow will be water, and the particles for the two-phase flow will be glass pellets with a diameter of 1.2 *mm*. The periodic behaviour will be evaluated by transferring the pressure gradient from the time domain to the frequency domain. This is to be done using Fast Fourier Transform. The drill string in the annulus section will also be rotated to observe the effect of the rotating drill string in the frequency domain. In addition to the evaluation of the periodic behaviour of the pressure gradient, an image processing algorithm is to be developed to analyse the images of particle flow patterns. The algorithm will be written as a graphical user interface (GUI) in Matlab and will assist to evaluate the liquid-particle flow.

2 Literature Review

2.1 PSD Analysis of Fluidized Beds

M'chirgui, Tadrist and Tadrist (1997) investigated pressure fluctuations in a fluidized bed to find a cause for the pressure fluctuations. Spectral analysis was performed on the time series of the pressure fluctuations. They found that the amplitude of the frequency signal would increase with an increase in the flow velocity of the gas, until the flow reached a slugging regime. Then, the amplitude would settle down and stabilize. This reduction in amplitude was found to be an indicator of a slug flow regime. Pressure fluctuations were also found to be linked to the changes of bed height. As the bed height increased, the pressure increased.

Johnsson, Zijerveld, Schouten, van den Bleek and Leckner (2000) performed time, frequency and state-space analysis on pressure fluctuations in fluidized beds. For the power spectrum analysis, a 200 *Hz* sampling frequency was used. It was found that the frequencies corresponding to flow regimes were all below 10 *Hz*. With regards to the dominant frequencies, the single bubble and exploding bubble regimes showed clear, narrow peaks, with the exploding bubble regime having a slightly higher frequency than the single bubble regime. This indicated a clear periodicity in the behaviour of the flow. While this periodic behaviour could easily be seen on the time signal for the single bubble regime, it was not apparent for the exploding bubble regime. The multiple bubble regime had a more spread out pattern in the power spectrum, with a noticeable peak at around 2.5-3 *Hz*. This spread-out nature was a result of the many different bubbles in the bed.

Felipe and Rocha (2004) studied the use of pressure fluctuations to identify different flow regimes, where the flow regimes were single bubble, multiple bubbles and slug flow. To do this, they used the signal analysis method Fast Fourier Transform (FFT) to transform the signal from the time domain to the frequency domain. The periodic variation in pressure could be seen in a pressure-time plot, where the variations were attributed to the oscillations in the bed of particles produced by the slug. The slug flow regime gave nice periodic variations. While the single bubble flow also showed periodic variation, it was nowhere near as smooth as the slug flow. The multiple bubble flow regime showed a more complex signal, where some of this complexity was attributed to the

variation in bubble sizes as the flow velocity of the bubbles varies with size. The amplitude of the signals would vary depending on the flow regime and would be proportional to the bubble size in the flow. Slug flow, with the largest bubbles, had the highest amplitude, while multiple bubble flow had the smallest bubbles and consequently the lowest amplitude. The FFT showed clear frequency responses for the periodic signal of the slug flow. Only one dominant frequency response could be seen. The single bubble flow also showed one dominant, narrow frequency response. The multiple bubble flow, however, showed several amplitudes with a wider frequency range than the other flow regimes. While there were several frequencies present, there was always one that was more dominant than the others. In their work, Felipe and Rocha (2004) did not find any significant differences between measuring differential pressure or absolute pressure.

He et al. (2013) used standard deviation and power spectrum analysis to process pressure fluctuations in a fluidized bed. This was done to investigate the dynamic behaviour of the transition from bubbling to the turbulent regime. For their experiments, they used two different kinds of non-spherical particles. The fine particles were found to have a stronger influence on the dynamic behaviour of the fluidized bed. Even when the fine and coarse particles were mixed with the same ratio, the characteristics of the fluidized bed tended towards the response of a pure fine particle response. In their study, they used an auto-regressive (AR) model for the power spectrum analysis, which was shown to give a smoother curve in the plot. In addition, the method showed a second frequency response that was not picked up by the traditional fast Fourier transform (FFT) method.

2.2 PSD Analysis of Pneumatic Conveying

Pahk and Klinzing (2008a) compared two different types of plastic pellets with the use of power spectral density (PSD) and wavelet signal analysis. The material for the pellets were hard, polystyrene pellets, and softer, more flexible polyolefin pellets. It was found that the average pressure drop was 3-4 times for polyolefin (soft material) than for polystyrene (hard material). The main reason was that the frictional pressure drop in the soft material was a lot higher than in the hard material. The solid friction factor decreased at the solid ratio was increased. During the experiments, the solid ratio was increased. With an increasing solid ratio, there could be seen an increase in the power of the frequencies in the range of 5-10 *Hz* for the polyolefin particles, and an

increase in the 10-15 *Hz* range for the polystyrene particles. This increase in power could be related to solid particle movement.

Pahk and Klinzing (2008b) investigated the relation of pressure fluctuations with regards to various flow regimes occurring in a dilute-phase pneumatic conveying system of industrial relevance. This was achieved by using four different signal analysis techniques, called power spectral density (PSD), rescaled range, phase space diagram, and wavelet analysis. The sample rate used was based on the Nyquist sampling-frequency and was chosen to be 1000 *Hz*. Also, the power spectrum converges faster when the number of data points is 2^N, so the data they acquired in each experiment was 2^{16} points. The PSD magnitude appeared to increase as the air velocity increased. When solids were introduced to the stream, a reduction in the amplitude of the turbulent signal could be seen compared to the turbulent signal without solids. This dampening effect would also increase as the concentration of solids was increased. During the rescaled range (RIS) analysis, it was found that the Hurst coefficient was the single-parameter that could distinguish between homogeneous and deposited-dune flow.

Vásquez, Jacob, Cocco, Dhodapkar and Klinzing (2008) analysed the effect of particles bouncing by visual inspection. For the experiments two different types of pellets were used, where all characteristics, like density, shape and diameter, except the hardness, were close to the same value. Results showed that the soft pellets had a higher pressure drop than the hard pellets. The soft pellets would bounce around a lot more than the hard ones. The increased pressure drop was in large parts thought to be due to the multiple times the particles had to be reaccelerated in the system. Also, the bouncing was thought to produce an increased drag force due to the different axial velocity of the air and the particles.

2.3 Liquid and Liquid-Particle Flow in Pipes

Takahashi, Masuyama and Noda (1989) investigated liquid-solid flow at low flow velocities. In their introduction, they mention that pressure loss in a flow with a moving bed is different from that of a deposited bed. Furthermore, the limit deposit velocity was found to be dependent on liquid-

particle density ratio, particle diameter, pipe diameter and solid concentration. In their study, they were able to find that the dune velocity would increase as the mean velocity of the mixture increased. The dune velocity to mean velocity ratio was found not to be dependent on the solid concentration. The solid concentration did, however, show an effect on the pressure fluctuations. Where solid concentrations up to 10 % were found to induce some increase in the pressure fluctuations, concentrations above 10 % had the reverse effect and would cause a decrease. This effect was attributed to the shape of the dune changing from peaks to flat. They performed power spectral density (PSD) analysis on the pressure fluctuation signal, where the PSD showed significant response below frequencies of 1 *Hz*. As the dominant frequency amplitude peaks increased with an increasing flow velocity, this lead to the conclusion that the pressure fluctuations were indeed related to the movement of the dunes.

McCann, Quigley, Zamora and Slater (1993) investigated the effect that high-speed rotation of the drilling string had in a narrow annuli. They conducted experiments with different kinds of fluids, both Newtonian and non-Newtonian, different degrees of eccentricity and with variations in flow rate and rotational speed. Pipe rotation was shown to have different effects on the pressure loss depending on the flow regime. The pressure loss for laminar flow decreased with an increase in rotation speed. Conversely, the pressure loss for turbulent flow increased with an increase in rotation speed. Also, an increase in mud, or fluid, rheology was found the increase the pressure loss for both types of flow regimes. It is also worth mentioning that the results showed the pressure drop decreased with an increased eccentricity for both flow regimes. Lastly, the results showed that when the drill pipe outer diameter to flow pipe inner diameter ratio was increased, the pressure loss increased.

Kim and Hwang (2003) studied how the pressure loss behaved in a concentric annulus with a rotating inner cylinder (drill string) under different flow conditions, from laminar to turbulent flow. The experiment was conducted with both a pure water phase and a 0.4 % CMC solution. The rotation speed of the inner cylinder was shown to increase the pressure losses for both water and the CMC solution. This effect was significantly larger in the laminar flow regime as opposed to the turbulent one. Also, the effect of the rotational speed was weaker in the CMC solution

Rabenjafimanantsoa, Time and Saasen (2005) performed a study on liquid-particle transport in a horizontal and inclined pipe, where the pressure drop was studied. The experiments were conducted using Newtonian (water) and non-Newtonian (PAC) fluids. At high flow rates, the non-Newtonian fluids showed higher pressure loss than the Newtonian one. Pressure fluctuations in the liquid-particle flow were contributed to the frictional pressure drop and from acceleration of the low flow area caused by the formation of dunes, as per the Bernoulli's equation. Visual inspection showed flow reversal downstream of the particle dunes, causing velocity and pressure fluctuations.

Rabenjafimanantsoa, Time, Hana and Saasen (2005) investigated the dune behaviour of liquid-particle flow using Ultrasound Velocity Profile (UVP) Monitoring instrument and Computational Fluid Dynamic (CFD) programs. The pressure along the dunes was shown to vary in accordance with the Bernoulli equation. The flow reversal downstream of the particle dunes could clearly be seen on the velocity profiles obtained. Also, the experimental results were shown to be in agreement with the numerical simulations done with CFD.

Woo, Kim, Kwon, Chung and Park (2011) studied the effect of a rotating cylinder, representing the drill string, on the transportation of cuttings in an annulus. They performed experiments on fully developed, laminar flow using both water and a water-based solution with 0.2 % sodium carboxyethyl cellulose (CMC). For particles, they used uniformly sized sand particles with a density of 2.55 g/cm^3. They found that the more viscous fluid could transport solids at a lower mixture velocity than water. It is also interesting to note that the pressure loss increased with the use of a more viscous fluid in the liquid-solid mix. Furthermore, the pressure loss increased with an increase in solids concertation and an increase in Reynolds number. This increase in pressure drop from higher volume fraction was contributed to the friction between the solids-wall or solids-solids.

3 Experimental Setup

This chapter contains detailed information about the equipment used in the experiments. The flow loop used in the experiments was a previous built medium-scale flow loop in the multiphase flow laboratory at the University of Stavanger. A symbolic diagram of the flow loop can be seen in Figure 3.1.

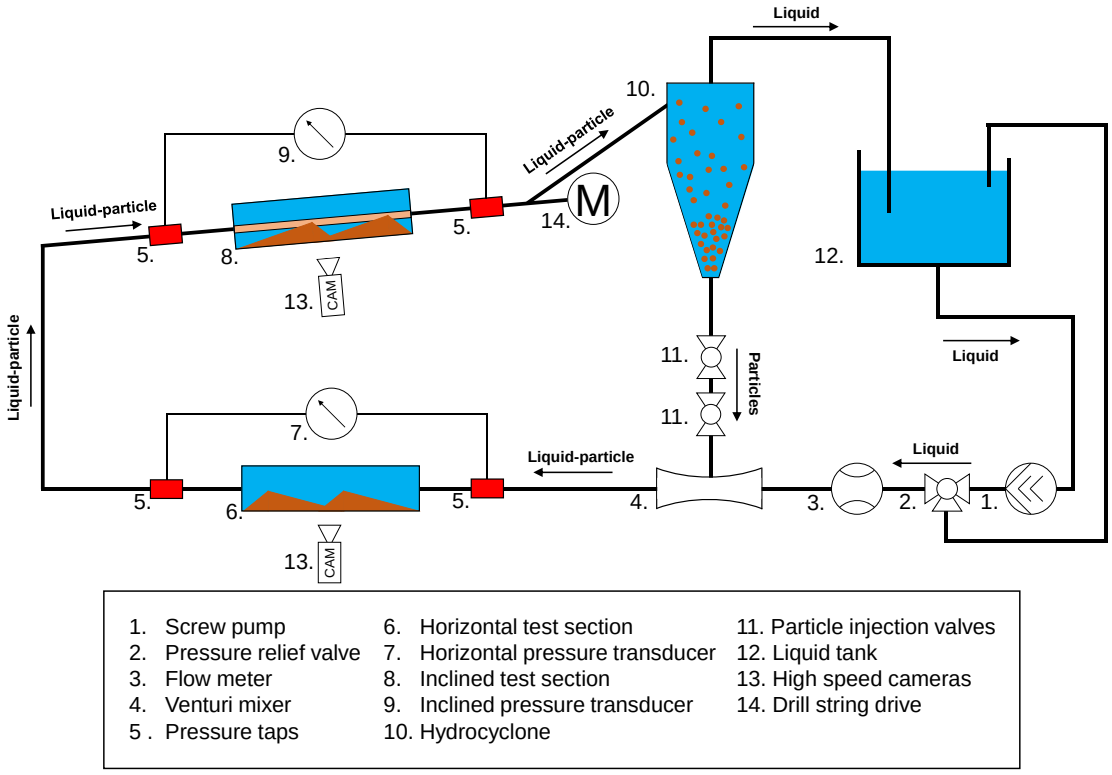

Figure 3.1 Symbolic diagram of the flow loop

3.1 The Flow Loop

The flow loop was made from transparent glass pipes with an inner diameter (ID) of 40 *mm* and a wall thickness of 2.3 *mm*. The pressure measurement cells (Rosemount 3051S transducers, item 7 and 9 in Figure 3.1) were connected to the flow loop through thin plastic capillary lines, filled with

water, that connected to the plastic pressure taps (items 5 in Figure 3.1) before and after each test section. These pressure taps did not disturb the inner diameter of the pipe.

The flow was initiated by a floor mounted screw pump (PCM Moineau 2515, item 1 in Figure 3.1). The output of the screw pump was controlled by a frequency inverter mounted on the wall. Normal operating frequencies for the pump were 3-15 *Hz*, which corresponded to a superficial liquid velocity, U_{sl}, of 0.17 – 0.90 *m/s* and an annular superficial liquid velocity, $U_{sl,a}$, of 0.28 – 1.57 *m/s*. The flow from the pump went through a T-shaped, 3-way ball valve (item 2 in Figure 3.1) which diverted some of the flow to a secondary pipe. This pipe acted as a pressure dampener to reduce the pressure fluctuation effect from the pump on the flow. Overflow from the pressure dampener was routed back to the liquid container.

The flow was lead through a Coriolis flowmeter (Promass 80F DN50, item 3 in Figure 3.1) that measured the mass flow rate of the liquid. From the flow meter, the flow was lead through a Venturi mixer (item 4. in Figure 3.1), where the particles were injected from the hydrocyclone (item 9 in Figure 3.1). There were two valves (items 10. in Figure 3.1) between the Venturi mixer and the hydrocyclone, to prevent pressure communication and flow diversion when injecting particles. Next, the flow went through the horizontal test section (HTS), where the differential pressure was measured. The pressure taps were spaced 1.52 *m* apart. The HTS was situated 4 *m* downstream of the injection point.

To get to the inclined test section (ITS), the flow went through a bend section, where there was an option to measure the differential pressure. The pressure taps in the inclined section (5° inclination from horizontal) were spaced 1.52 *m* apart, along the length of the pipe. The ITS is illustrated in Figure 3.2. In this section, a drill string (DS) was inserted into the glass pipe, with the DS having an outer diameter (OD) of 25 *mm*. The DS was made up of three sections, with flexible joints between them. The total length of the DS was 4.62 *m*. One end was loose, while the other was fixed to the drive unit which controlled the rotation of the DS. The drive unit was made up by three pieces, a gearhead (GPX 22 C), a motor (DCX 22 L) and an encoder (ENX 16 Easy), delivered by Maxon Motor. The rotation speed (ω) of the DS was controlled using the software Escon.

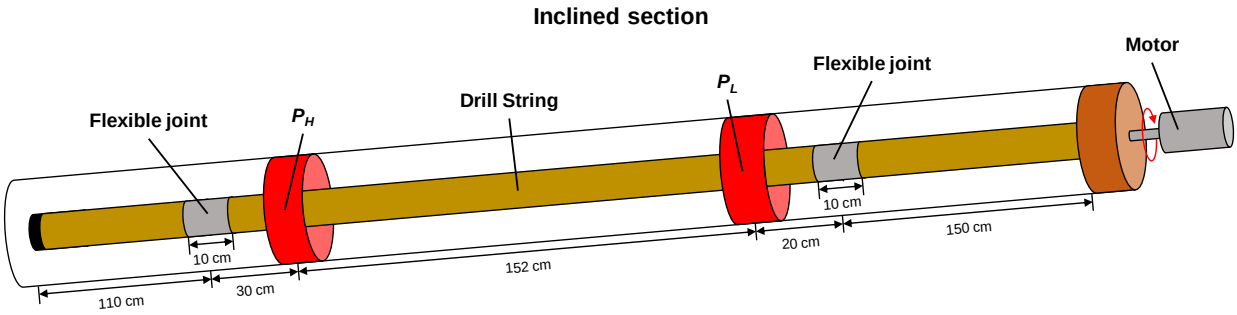

Figure 3.2 Illustration of the inclined section

The flow then went through an even more inclined section (35° inclined from horizontal), which also had the option for measuring the differential pressure. The total length of the test sections was about 13 *m*. From the inclined section, the flow was lead to the hydrocyclone, where the particles were separated from the flow and reinjected to the test sections. Finally, the pure liquid flow was lead back to the liquid container (items 11. in Figure 3.1), finalizing the closed flow loop.

3.1.1 Video recording

Both test sections were encased by a rectangular box, filled with water, to prevent optical diffraction of the light while doing the video recordings. To record the particle flow on images, two cameras were used. One was positioned to record the HTS and one was positioned to record the ITS. A Basler acA800-510um camera was used for the HTS, with capabilities of a frame rate of 500 *fps* at its full resolution of 800 *px x* 600 *px*, in grayscale video. For the ITS, a Basler acA800-510uc was used to record, with capabilities of a frame rate of 500 *fps* at its full resolution of 800 *px x* 600 *px*, in colour video. To increase the contrast of the images, a uniform white light-emitting diode (LED) panel was used as a backlight in each of the test sections. The software Pylon Viewer was used to record and save the video.

3.1.2 Pressure recording

The differential pressure was recorded by up to four Rosemount 3051S transducers. During the experiments, two transducers were used; one to record the HTS and one to record the ITS. The pressure transducers were set to record in the range from -62 *mbar* to 62 *mbar* in the HTS and from

-620 *mbar* to 620 *mbar* in the ITS. The pressure was recorded in the program LabView and stored as text (.txt) files. The mass flow rate and ambient temperature were also recorded and stored in the same text file.

3.2 Particles

The particles used for the experiments were glass pellets supplied by the Glaswarenfabrik Karl Hecht. The average diameter of the particles was found by taking pictures of the pellets in a microscope. The pictures were processed in Matlab using the integrated Image Viewer app. The diameter of each particle was measured with the Measure Distance tool in Image Viewer, returning the diameter in pixels. The diameter was then converted from pixels to *mm*, using the scale shown in Figure 3.3. The average diameter of the particles was found to be 1.17 *mm* ± 0.10 *mm*.

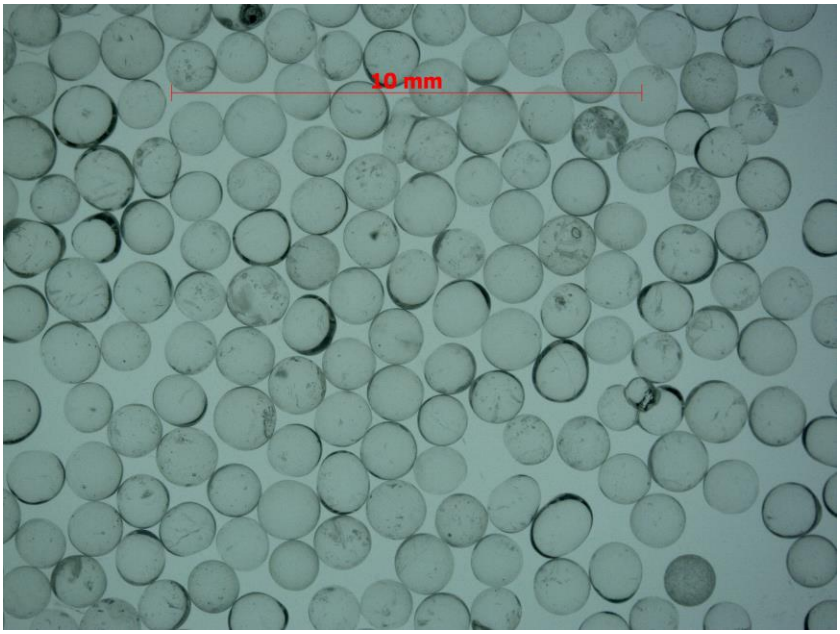

Figure 3.3 Picture showing a representative sample of particles

3.3 Operational Procedure

The flow was initiated by starting the frequency inverter. At first, the flow loop was run at low liquid velocities. The velocity was then carefully ramped up to the maximal safe velocity. The flow was held at this velocity for at least 30 minutes, to allow for air to escape the system. During this ramp-up phase, the capillary lines connected to the pressure transducers were also flushed, using a system connected to a water tap. Once the air had been satisfactorily removed from the system, the test phase began.

3.3.1 Steady-state testing

For the steady-state testing, the system was run at the flow velocity for the following test until the differential pressure stabilised, for a minimum of 5 minutes. Once the system was stable, the pressure recording was started. For liquid flow, the recordings were run for at least 2 minutes. For the liquid-particle flow, the particles were injected once the liquid flow had stabilised and the recordings were run for as long as it took for the particles to leave the system. The steady-state testing was performed on both the horizontal and the inclined test section.

3.3.2 Dynamic testing

For the dynamic state test, a limited number of particles was injected to the flow and allowed to settle about a metre downstream of the Venturi mixer, where the flow was shut off. The recordings start once the flow was restarted. The flow was started directly at a certain flow velocity, and the recordings were taken until the particle dune passed the low side pressure tap, P_L. The dynamic test was only performed in the horizontal test section.

4 Methodology

This chapter will describe the method used for the frequency spectrum analysis and the methods used in the image processing. The post processing of the differential pressure signals and the images from the high-speed cameras was performed using the MATLAB software, supplied by MathWorks.

4.1 Power Spectral Density

4.1.1 Fourier transform

The Fourier transform is a useful tool to evaluate the periodic behaviour of a signal in the time domain. The signal is transformed from the time domain to the frequency domain. This can easily be observed in an ideal sinusoidal signal, as is the case in Figure 4.1a. This signal has an amplitude of 10 and a frequency of 5 *Hz*. When the Fourier transform is applied, both the amplitude and frequency can be distinguished in the frequency domain, as shown in Figure 4.1b. The beauty of the Fourier transform can be observed when looking at Figure 4.1c and d, where both a second sinusoidal component, with an amplitude of 10 and frequency of 2 *Hz*, and a random noise has been added to the signal in Figure 4.1a. While it is near impossible for the human mind to separate the two sinusoidal components in the time domain, the frequency can be seen with ease in the frequency domain.

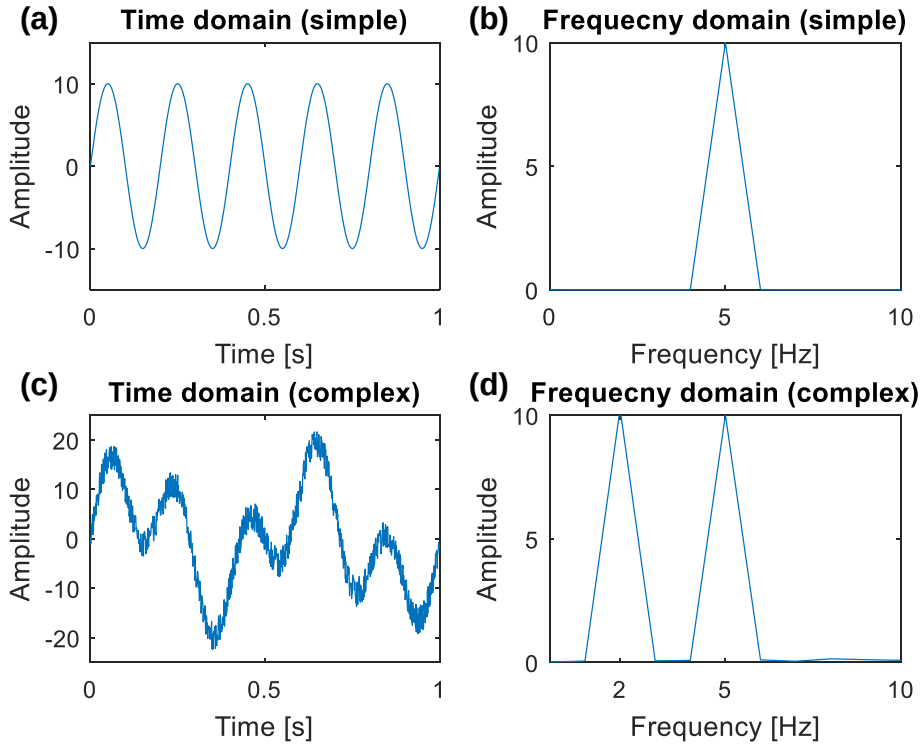

Figure 4.1 Comparison of time and frequency domain of a simple and a complex signal

The Fourier Transform of a continuous signal *f(t)* is given by (Roberts, 2003)

$$F(j\omega) = \int_{-\infty}^{\infty} f(t)e^{-j\omega}dt \tag{4.1}$$

For *N* samples of *f(t)* separated by the sample time *T*, where the samples are denoted *f(0),f(1),…,f(k),…,f(N-1)*, the Fourier transform can be written as

$$F(j\omega) = \sum_{k=0}^{N-1} f(k)e^{-j\omega kT} \tag{4.2}$$

The Discrete Fourier Transform (DFT) treat the data as if it were periodic and is therefore evaluated for the fundamental frequency and its harmonics, where

$$\omega = 0, \frac{2\pi}{NT}, \dots, \frac{2\pi}{NT} \cdot 2, \dots, \frac{2\pi}{NT} \cdot n, \frac{2\pi}{NT} \cdot (N-1)$$

The general DFT can then be written as

$$F(n) = \sum_{k=0}^{N-1} f(k) e^{-j\frac{2\pi}{N}nk}, n = 0,1, \dots, N-1 \quad (4.3)$$

In the literature, there are three common scaling factors for the DFT (Heinzel, Rüdiger and Schilling, 2003)

$$y_m^{(1)} = \sum_{k=0}^{N-1} f(k) e^{-j\frac{2\pi}{N}nk} \quad (4.4)$$

$$y_m^{(2)} = \frac{1}{\sqrt{N}} y_m^{(1)} \quad (4.5)$$

$$y_m^{(3)} = \frac{1}{N} y_m^{(1)} \quad (4.6)$$

The Fast Fourier Transform (FFT) uses an optimised algorithm to calculate the DFT.

4.1.2 PSD based on FFT

Matlab uses the DFT defined by $y_m^{(1)}$ for calculating the FFT (Kandhasamy, 2010). The PSD is calculated by squaring the DFT and applying the correct normalization factor. As the interest in this thesis is the power of the signal, a normalization factor of 1/*N* is used for the FFT. This is done to make the FFT independent of the signal length. For creating the PSD in Matlab, the FFT is first calculated from the signal, *X* ("Fast Fourier Transform," n.d.):

≫ Y = fft(X);

Next, the two-sided amplitude spectrum is defined:

≫ P2 = abs(Y);

The single-sided amplitude is then created by extracting the values corresponding to the response from the frequency 0 and up to and including the Nyquist frequency:

≫ P1 = P2(1:N/2+1);

The PSD is then calculated by squaring the single-sided amplitude spectrum. In this step, the correct scaling factors are also applied. In this case the output wanted is Pa^2/Hz, where the magnitude of the power is of interest. This is obtained by dividing the PSD by N^2. As the two-sided amplitude spectrum displays half the energy at the positive frequency and half the energy at the negative frequency, the single-sided PSD must also be multiplied by 2 to correct for this, at all frequencies except 0 (DC) and the Nyquist frequency:

≫ PSD = P1.^2/N^2;
≫ PSD(2:end-1) = 2*PSD(2:end-1);

4.2 Image Processing

The flow loop was set up with a backlight and a camera in the test sections, as described in chapter 3, to capture the particle flow patterns. The processing of the images uses the concept of bed compaction to distinguish between a static layer and a moving layer. As the static layer is not moving, it will be more compact than the moving layer. This means that the static layer will let through less light than the moving layer to the camera, and it follows that the static layer will be darker than the moving layer. Figure 4.2 shows an example of a grayscale image captured by the camera. The grayscale varies from 0 to 255, where 0 is black and 255 is white colour.

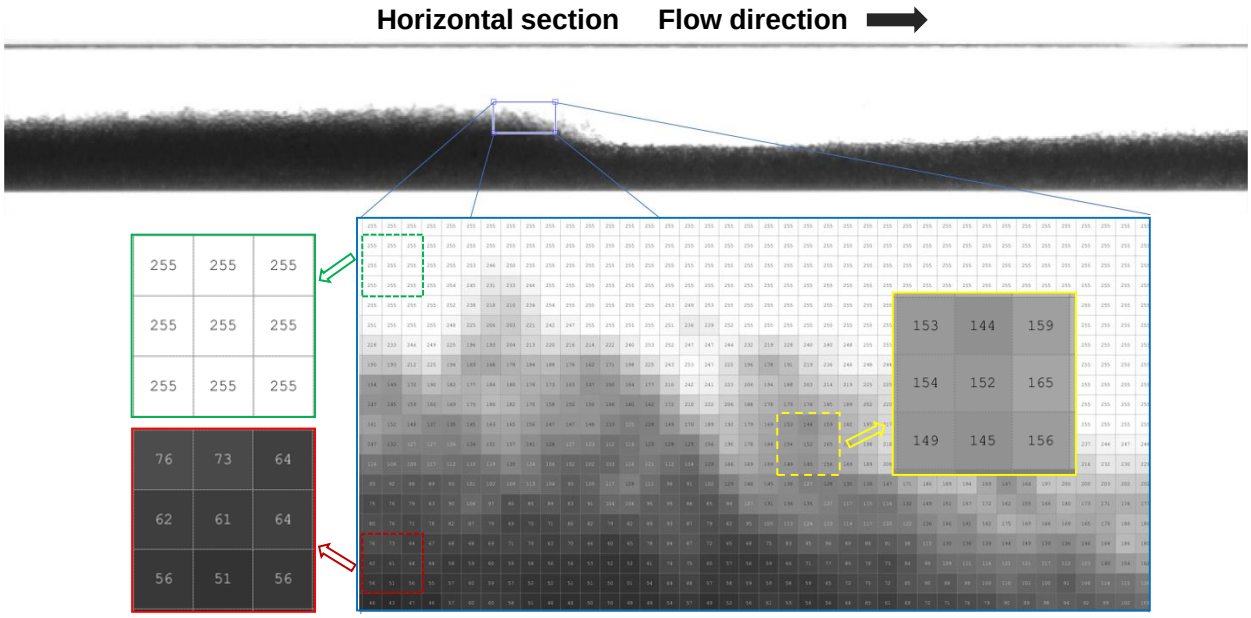

Figure 4.2 Picture showing grayscale intensities

To process the images a Graphical User Interface (GUI) was written in Matlab. Figure 4.3 shows the flowchart of the GUI.

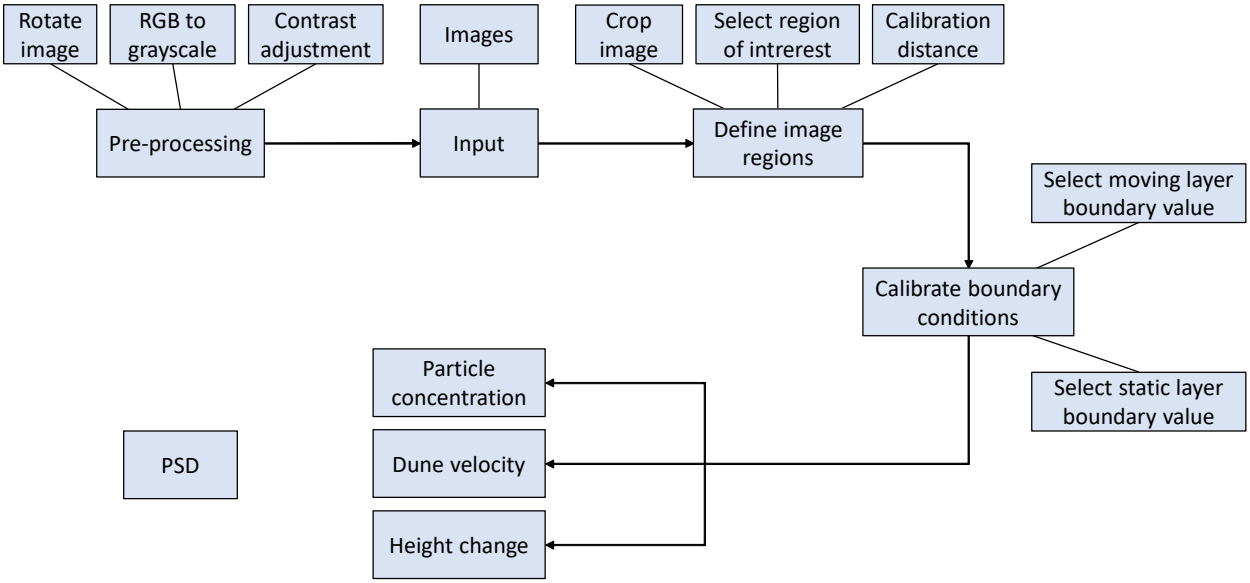

Figure 4.3 Image processing flowchart

4.2.1 Pre-processing

For increasing the accuracy of the image processing, some pre-processing of the images has to be done on the raw images. The first one is to rotate the images. Selecting the region of interest (ROI) is very sensitive to a non-horizontal pipe. Therefore, it is essential to adjust the images to a horizontal position in order to increase the accuracy of the calculations. For cameras recording in colour it is also necessary to convert the images to grayscale.

4.2.2 Define image regions

After inserting the images to the GUI, the first step is to define some essential regions and distances. Cropping the image is done to make the image more manageable and to speed up the computing. A region of interest is defined to ease the processing of the images. This bypasses difficulty encountered with for example the pipe being interpreted as a part of the bed. A calibration distance is also selected. This is a distance where the length is known, for example the inner diameter of the pipe. This distance is later used to convert the units from pixels to millimetres.

4.2.3 Calibrate boundary conditions

Calibration of the boundary conditions is done before the results are calculated. The calibration is done by selecting the grayscale intensity values by which the static and moving layer will be sorted. For example, a static layer with boundary values of 0-97 will define the static layer as pixels where the grayscale intensity is between 0 and 97. The selection of boundary values can be previewed, and a satisfactory definition of the static and moving layer is subject to individual evaluation. The process can be seen in Figure 4.4. Binary images are made of both the static and the moving layer, then they are combined into a two-colour image, where the static layer is black and the moving layer is gray. This image is then used as a basis for identifying the boundaries of the layers, and they are then drawn on the original image, where the boundaries can be seen.

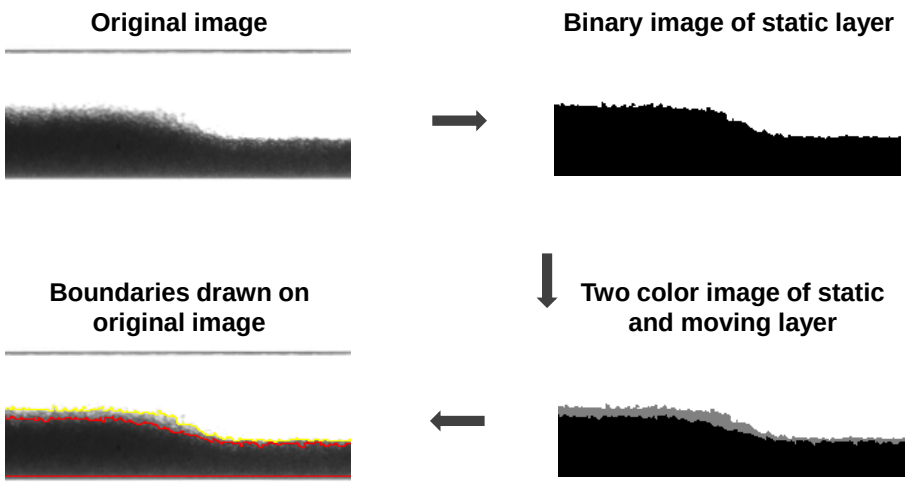

Figure 4.4 Process of identifying the static and moving layer

4.2.4 Output

The results are calculated after the boundary values have been defined. There are three different outputs produced by the GUI. The outputs are particle concentration, dune velocity and change of the bed height.

Particle concentration. The particle concentration of each layer is calculated based on the binary images of separate layers and return a particle concentration of the static and moving layers. The boundary obtained in Figure 4.4 is divided into *n* segments, where *n* is the width of the region of interest defined in an earlier step. By assuming a horizontal spread of the particles in the pipe, a cross section of the pipe containing particles can be made. First, the moving layer boundary is used to calculate the cross-sectional area occupied by both layers. Then, the static layer boundary is used to calculate the cross-sectional area occupied by the static layer. The area of the static layer can then be subtracted from the area of both layers, giving the cross-sectional area of the moving layer. The process is shown in Figure 4.5.

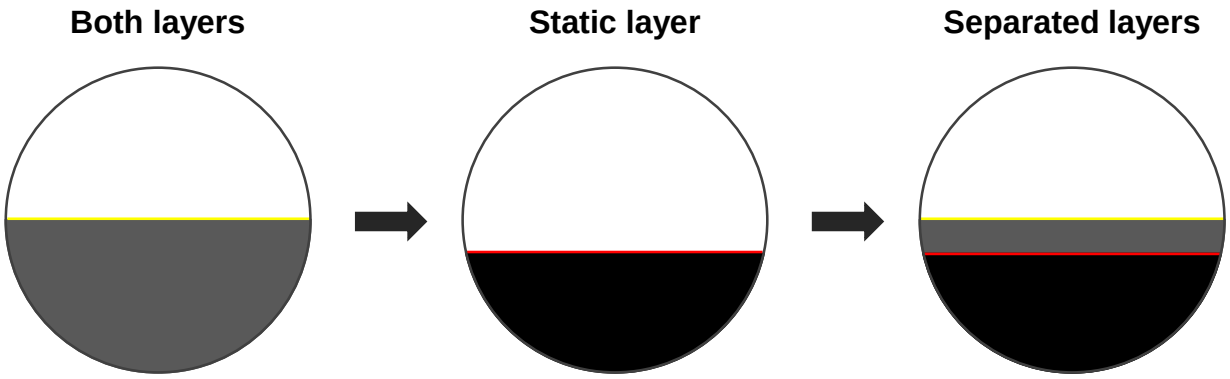

Figure 4.5 Process of defining the area of the moving and static layers for a cross section

This process is then repeated *n* times, for the entire length of the image, giving the volume of each layer. The volume concentration is then calculated by dividing the volume of the particles by the volume of the pipe. The static layer particle concentration, $C_{p,sl}$, is given by:

$$C_{p,sl} = \frac{1}{V_{pipe}} \sum_{k=1}^{n} (A_{sl})_k \tag{4.7}$$

Where V_{pipe} is the volume of the pipe and A_{sl} is the cross-sectional area of the static layer. Similarly, the moving layer particle concentration, $C_{p,ml}$, is given by:

$$C_{p,ml} = \frac{1}{V_{pipe}} \sum_{k=1}^{n} (A_{ml})_k \tag{4.8}$$

Where A_{ml} is the cross-sectional area of the moving layer.

Dune velocity. The dune velocity is calculated from the boundary of the entire bed. The boundary is converted from a binary image to a function. The process is visualised in Figure 4.6. A binary image is created from the grayscale image of the bed. Then, the binary image us used to find the boundary of the bed. Finally, the boundary is used to create a function of the height of the bed.

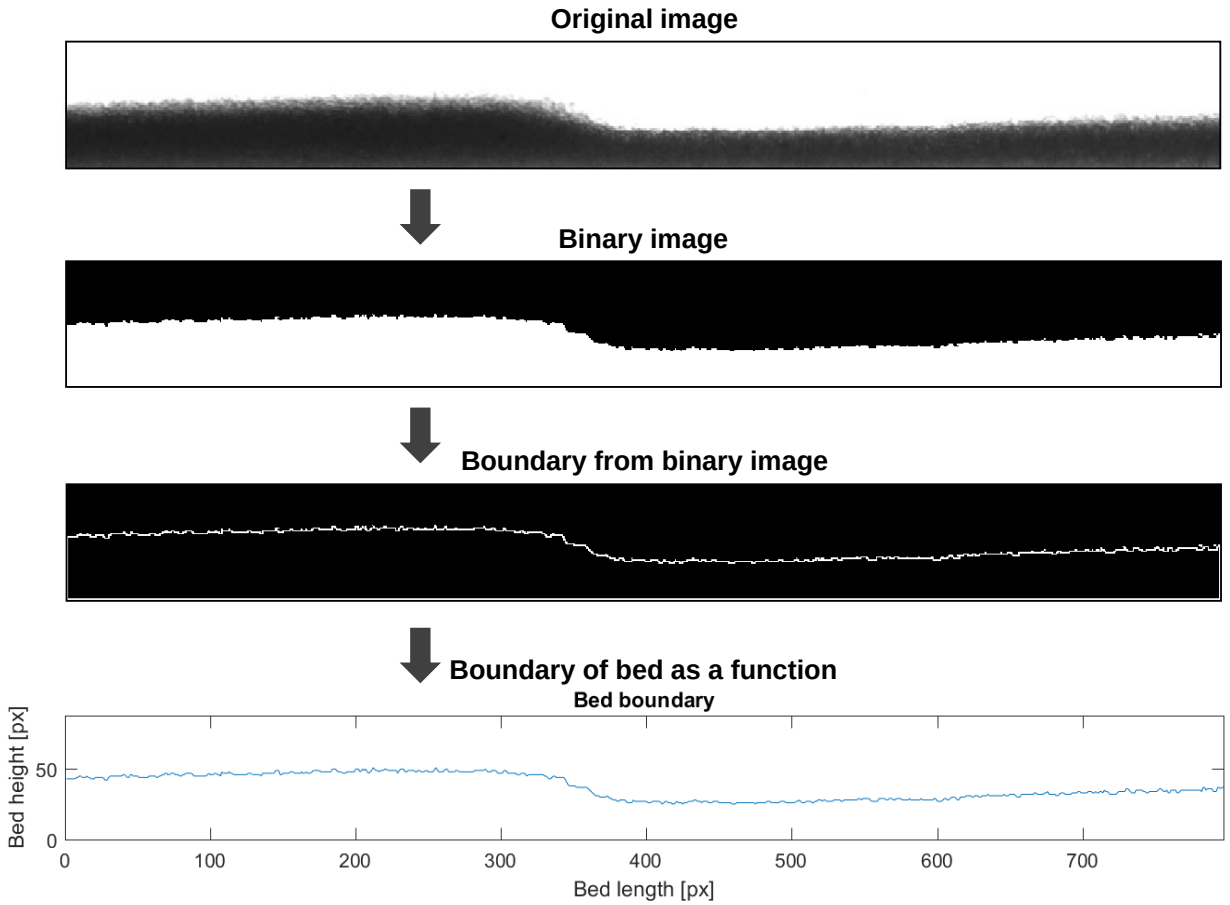

Figure 4.6 Process of finding the boundary of the bed as a function to use in cross-correlation

A cross-correlation between functions at two different times is then made. An example is shown in Figure 4.7. By knowing the time difference between the two images, defined by the frames per second (FPS) of the recording and the real distance of one pixel, defined by the calibration distance, it is a small matter to find the velocity of the dune.

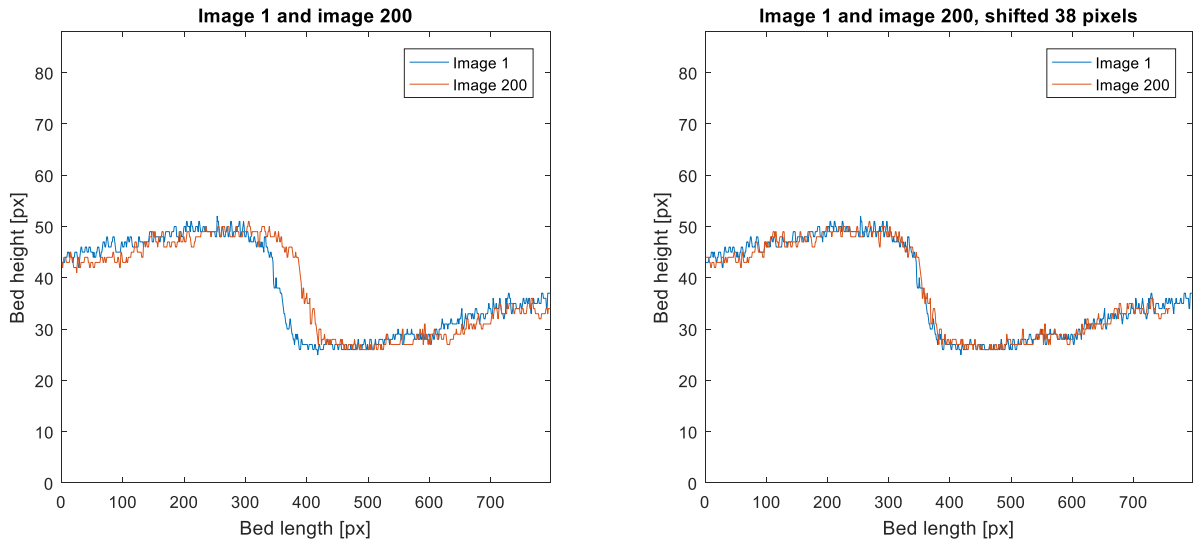

Figure 4.7 Cross-correlation of image 1 and 200 in a series

Height change. The binary images are used to calculate the changes in area and height in a picture series. This is done by counting the number of pixels occupied by particles in a fixed window. The changes in area are converted to changes in height by dividing the area change by the window width. This is illustrated in Figure 4.8, where a window with a width of 50 pixels has been chosen. The number of white pixels is then counted, giving an area in px^2. Using the calibration distance defined earlier the area is transformed to cm^2.

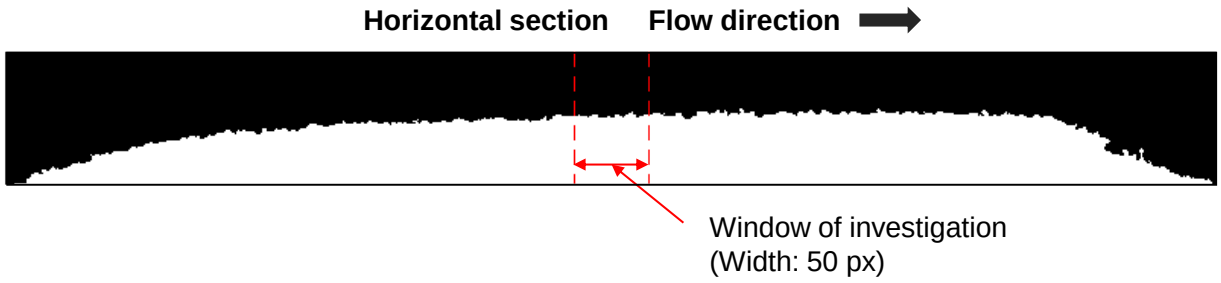

Figure 4.8 Window of investigation for area and height analysis

5 Results and Discussion

5.1 Pressure Gradient and PSD

The first experiments were run with only liquid flow, in this case water, to calibrate the equipment and to establish a baseline behaviour of the pressure gradient in a pure liquid flow. Also, the effect of the drill string (DS) rotation on the differential pressure was evaluated. Differential pressures were recorded in the horizontal and inclined section. In the horizontal section, there was no DS and it follows that the flow during the recordings was a pipe flow. In the inclined section, a DS was present during all the pressure recordings. Thus, the flow during the experiments was an annular flow. The flow regime for all superficial liquid velocities was turbulent.

5.1.1 Horizontal test section (pipe flow)

Figure 5.1 shows the differential pressure recordings of a liquid flow (a) and a liquid-particle flow (b) at the same superficial liquid velocity, U_{sl}, of 0.35 *m/s*. The pressure gradient is shown on the y-axis and the time on the x-axis. By visual observation, small amplitude peaks can be seen in the liquid flow, indicating some form of periodic behaviour of the pipe flow.

The liquid-particle flow (Figure 5.1b) is showing a greater variation than the liquid flow. The time domain plot shows significant amplitude peaks and low points. The same shape appears to be repeating several times during the recorded interval.

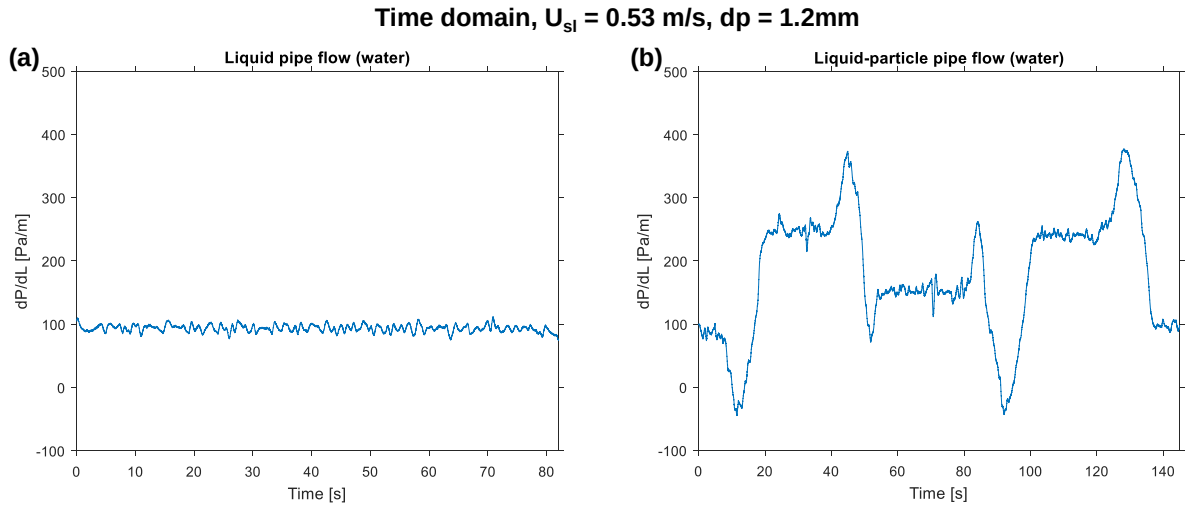

Figure 5.1 Pressure gradient in the horizontal section at U_{sl} = 0.53 m/s for **a)** liquid pipe flow and **b)** liquid-particle pipe flow

The same behaviour can be seen when increasing the superficial liquid velocity, U_{sl}, to 0.71 *m/s* (Figure 5.2). The liquid flow (Figure 5.2a) has the same pattern for the recording, but a higher pressure gradient, as is to be expected due to the frictional pressure drop increasing with an increasing U_{sl}. In the liquid-particle flow (Figure 5.2b), similar peaks and lows can be seen in the plot of the signal as was observed for the liquid-particle flow at a U_{sl} of 0.53 *m/s*. One noticeable difference is the peaks are occurring more frequent at the higher U_{sl}.

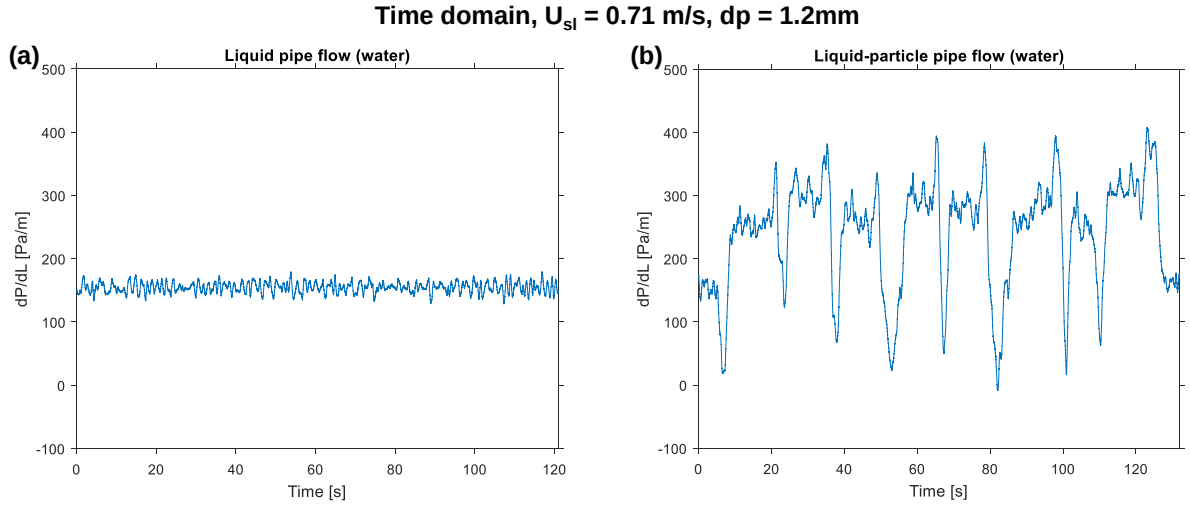

Figure 5.2 Pressure gradient in the horizontal section at U_{sl} = 0.71 m/s for **a)** liquid pipe flow and **b)** liquid-particle pipe flow

Both Figure 5.1b and Figure 5.2b displays negative pressure gradients. This can be explained by the Bernoulli's principle. As the dune moves through the pipe, the flow area for the liquid is reduced. When this happens, the kinetic energy of the fluid increases at the expense of the pressure in the fluid. As a result, a minimum pressure in the fluid can be seen at the maximum height of the dune. The dune moves through the pipe and passes the high side pressure tap, P_H (left pressure tap in Figure 5.3a and b) and the low side pressure tap, P_L (right pressure tap in Figure 5.3a and b). The minimum value of the pressure gradient can be seen when the dune passes the high side pressure tap. Similarly, the maximum value can be seen when the dune passes the low side pressure tap.

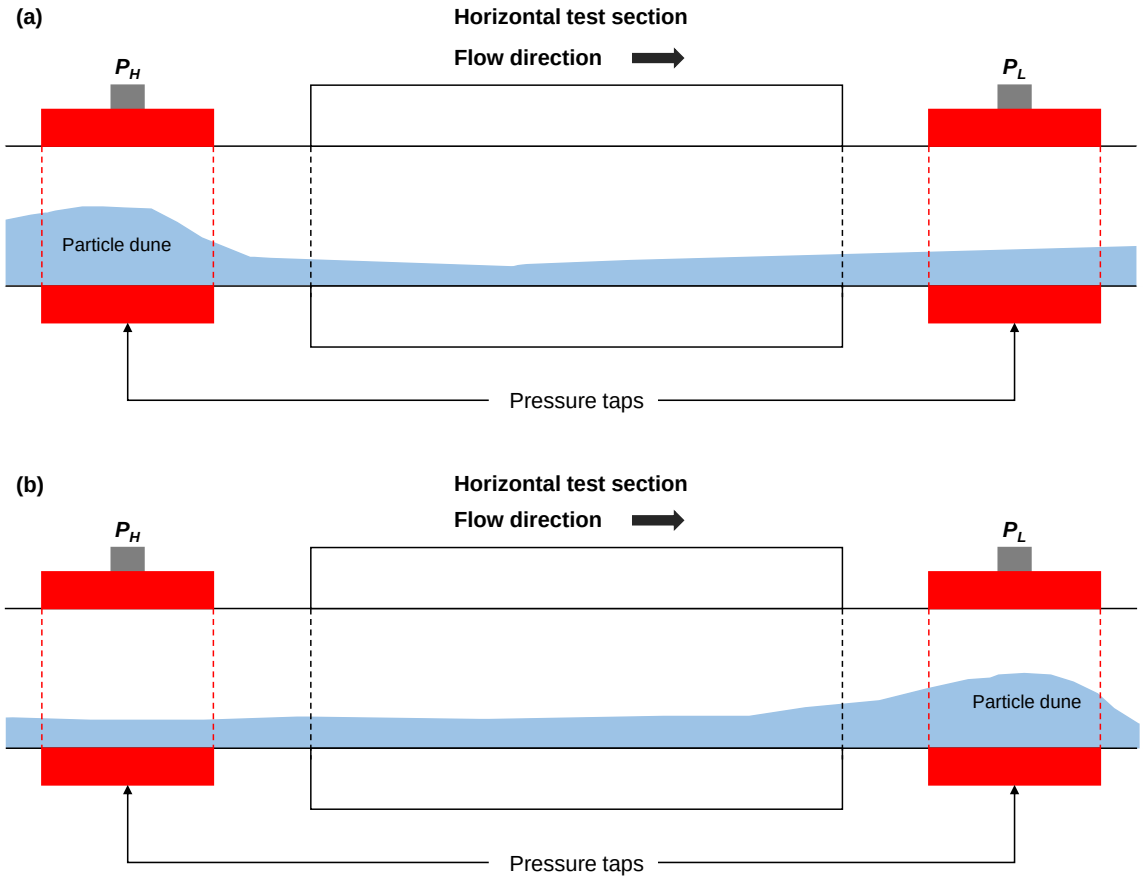

Figure 5.3 Illustration of liquid-particle flow in the horizontal test section, where **a)** The particle dune is passing the high side pressure tap, P_H **b)** The particle dune is passing the low side pressure tap, P_L

The more frequent occurrence of peaks at a higher U_{sl} can then be explained by dunes moving faster through the pipe, indicating better hole cleaning.

The periodic behaviour of the pressure gradient is shown more clearly once the PSD analysis has been done. This is shown in Figure 5.4, where the power corresponding to each frequency is shown on the y-axis and the frequency is shown along the x-axis. The liquid flow (Figure 5.4a) shows several peaks at frequencies below 1.5 *Hz*. Their small amplitude reflects the low variance of the pressure gradient in Figure 5.1a. The PSD analysis of the liquid-particle flow (Figure 5.4b) shows a few dominant frequencies below 0.1 *Hz*.

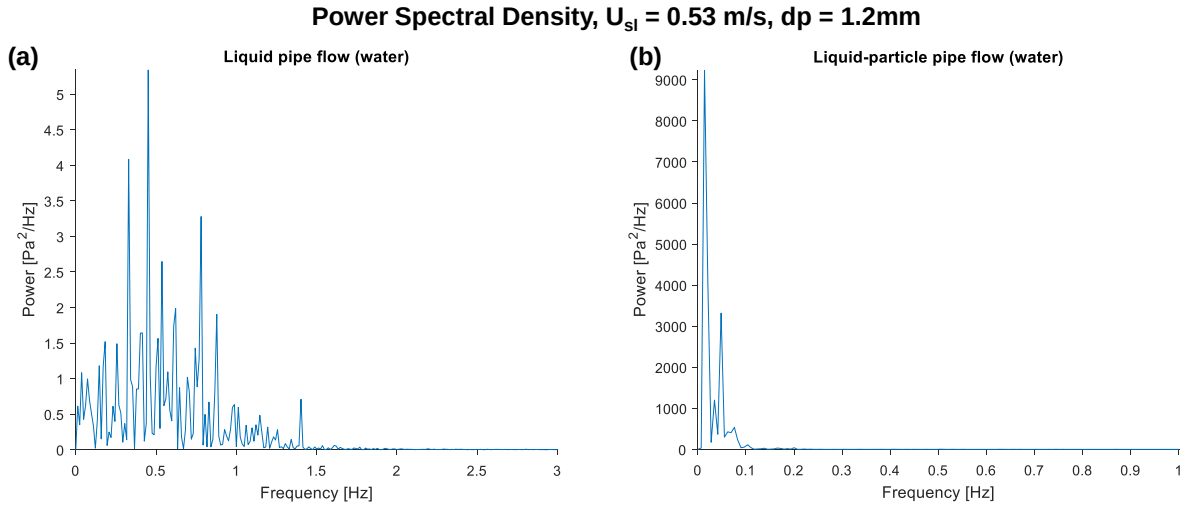

Figure 5.4 PSD of the horizontal section at U_{sl} = 0.53 m/s for **a)** liquid pipe flow and **b)** liquid-particle pipe flow

The similarities between the liquid flow at different U_{sl} become more apparent when observing the PSD plots (Figure 5.4a and Figure 5.5a) of both. Both the magnitude of the peaks and the shape of the PSD are similar, indicating the flow is behaving in the same way. Similarly, the differences of the liquid-particle flows can also be observed in the PSD (Figure 5.4b and Figure 5.5b). Where the low U_{sl} displays a few high peaks at very low frequencies, the higher velocity has several low peaks spread over a wider range of frequencies, with the dominating frequencies being under 0.4 *Hz*.

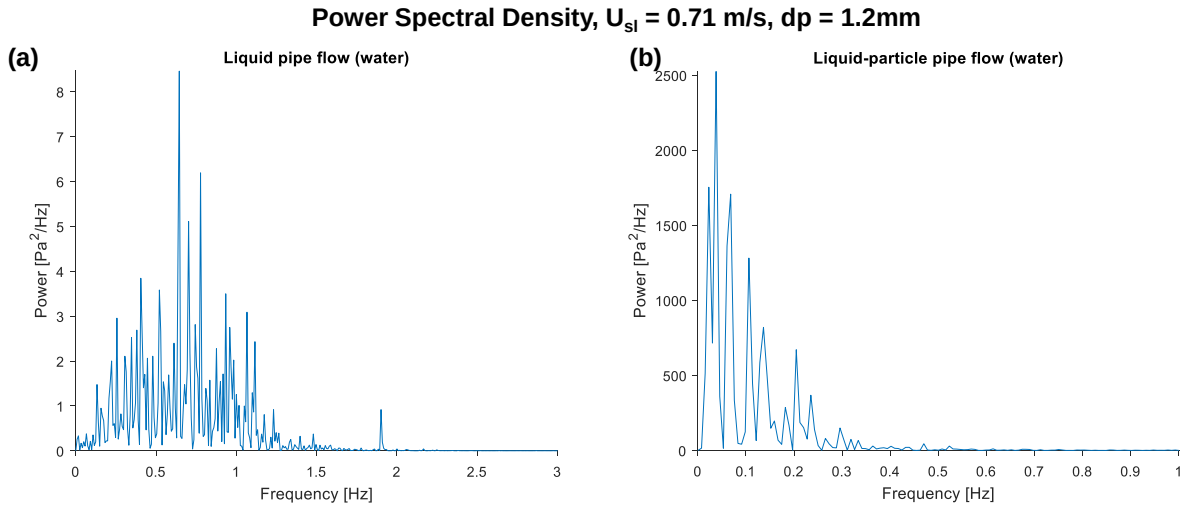

Figure 5.5 PSD of the horizontal section at U_{sl} = 0.71 m/s for **a)** liquid pipe flow and **b)** liquid-particle pipe flow

5.1.2 Inclined test section, 5° from horizontal (annular flow)

Figure 5.6 shows the pressure gradient at an annular superficial liquid velocity, $U_{sl,a}$, of 0.78 *m/s*. The left side plots (a, c, e) show an annular liquid flow at different RPMs (0, 20 and 100) while the plots on the right (b, d, f) show an annular liquid-particle flow at different RPMs (0, 20 and 100). The pressure gradient is shown on the y-axis and the time is shown on shown on the x-axis.

As with the horizontal section, the liquid flow (Figure 5.6a) show some periodic behaviour. The introduction of rotation to the DS is clearly reflected in the differential pressure measurements (Figure 5.6c). The signal appears as a nearly perfect sinusoid, where the RPM can be counted by the peaks on the signal. A trend that is also apparent by observing the pressure gradient while rotating the DS is that the pressure gradient increases as the RPM is increased. This agrees well with results reported by McCann et al. (1993) and Kim and Hwang (2003), where the pressure loss was found to increase with an increasing RPM of the inner cylinder in turbulent flow.

The liquid-particle flow shows no distinguishable difference between the different rotations (Figure 5.6b, d and f). The same periodic high values can be seen throughout.

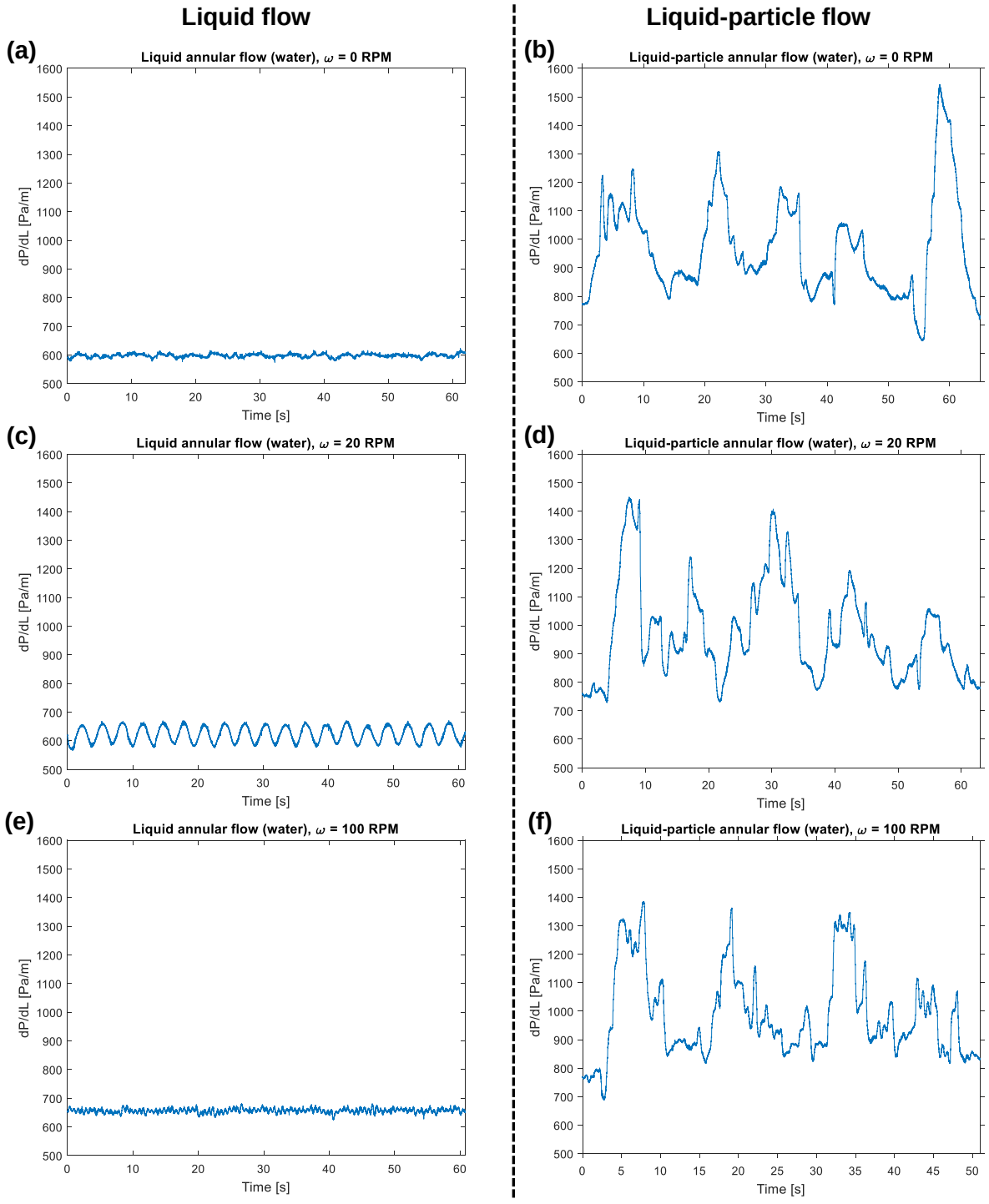

Figure 5.6 Pressure gradient in the inclined section for **a, c, e)** liquid annular flow and **b, d, f)** liquid-particle annular flow at $U_{sl,a}$ = 0.78 m/s

Figure 5.7 shows the PSD analysis of liquid (a, c, e) and liquid-particle (b, d, e) flows of an annular superficial liquid velocity, $U_{sl,a}$, of 0.78 *m/s* with different RPMs (0, 20 and 100). The power corresponding to each frequency is shown on the y-axis and the frequency is shown along the x-axis.

The annular liquid flow without rotation (Figure 5.7a) show the same behaviour as the liquid pipe flow (Figure 5.4a) in the frequency domain. Low amplitude peaks, mainly ranging from *0* to *1.5 Hz* represents the flow. The rotation of the DS can be seen even more clearly in the frequency domain than in the time domain. At a rotational speed of ω = 20 *RPM* the differential pressure signal displayed a clear sinusoidal nature (Figure 5.6c). This sinusoid can easily be observed in the PSD plot, as shown in Figure 5.7c. The PSD analysis returned a single clear peak at 0.33 *Hz* (20 *RPM* = 0.33 *Hz*). The same can be seen in Figure 5.7e, for a rotation speed of ω = 100 *RPM*. Also, it is noted that the amplitude of the PSD reflects the variance of the gradient. The signal shows high variance at low RPM, which results in a high amplitude of the peak in the PSD plot. Similarly, the high RPM signal shows a lower variance and a corresponding lower amplitude.

The entering of particles to the annular flow caused immediate changes to the PSD, just the same as with the pipe flow. A single, high amplitude can be seen at frequencies below 0.5 *Hz* (Figure 5.7b). The frequency response of particles movements is so strong compared to the rotation of the DS that the response from the DS is barely visible. At a rotational speed of ω = 20 *RPM*, a relatively low amplitude peak can be seen at the expected frequency of 0.33 *Hz* (Figure 5.7d). As can be observed in the annular liquid flow, the high rotation speed (100 *RPM*) has a low amplitude response. This is also true for the case of the annular liquid-particle flow (Figure 5.7f). The amplitude response of the DS is barely visible at the expected frequency of 1.67 *Hz*.

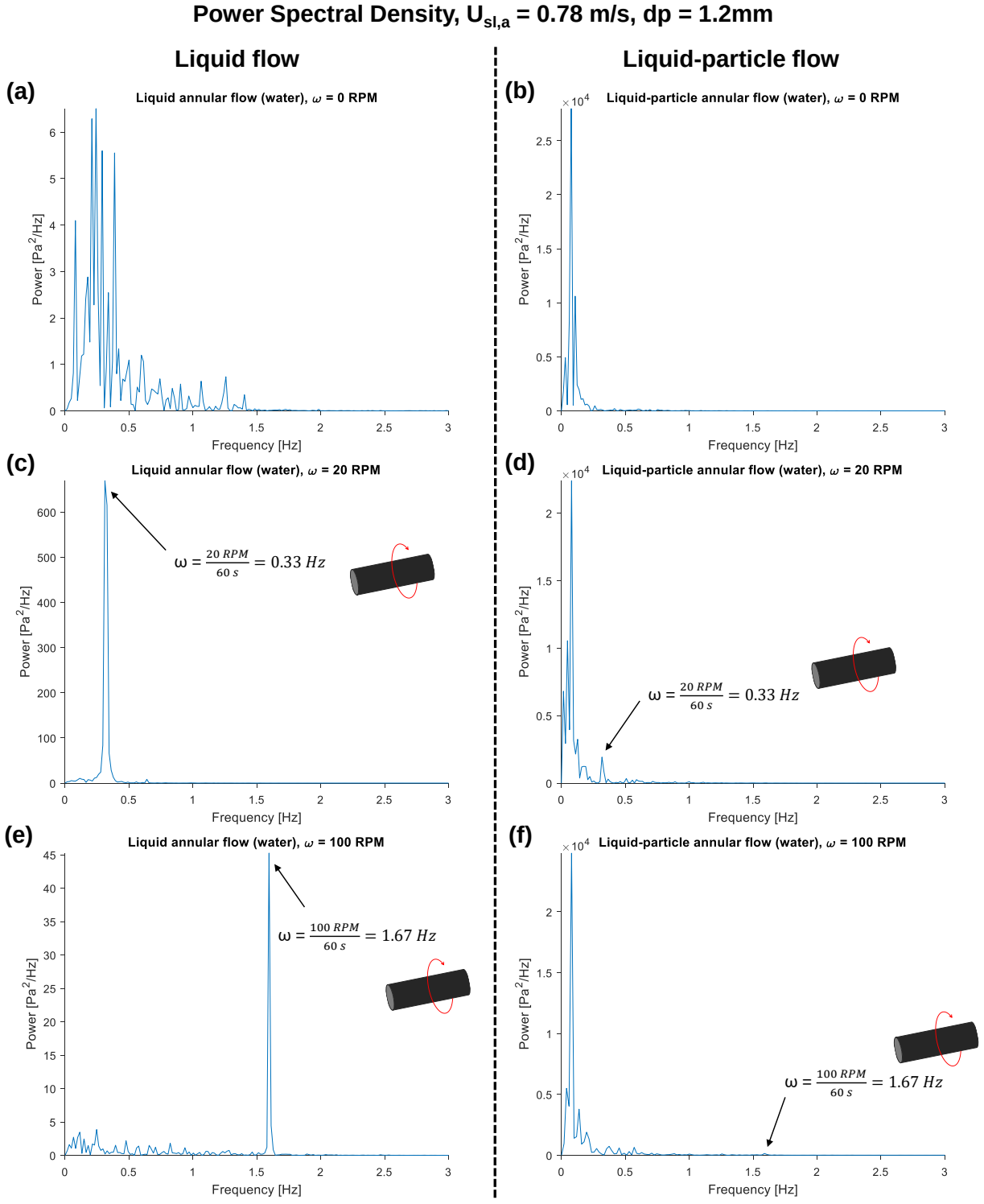

Figure 5.7 PSD of the inclined section for **a, c, e)** liquid annular flow and **b, d, f)** liquid-particle annular flow at $U_{sl,a}$ = 0.78 m/s

5.2 Particle Dune Images

Due to challenges imposed by the DS in the ITS, the image processing was only performed on images taken in the HTS. This also simplified the calculations as the horizontal and vertical movement was in the same x- and y-plane as the camera.

In this thesis, three cases will be presented. Two steady state tests at U_{sl} of 0.41 *m/s* and 0.71 *m/s* respectively, and a dynamic test at U_{sl} of 0.47 *m/s*. Figure 5.8 shows a few selected frames of the steady-state test at U_{sl} of 0.41 *m/s*, recorded at a frame rate of 500 *fps*. The flow is fully developed, with a continuous bed and a moving layer. The flow rate is low, and frame rate of recording is high, so there are very little changes from frame to frame.

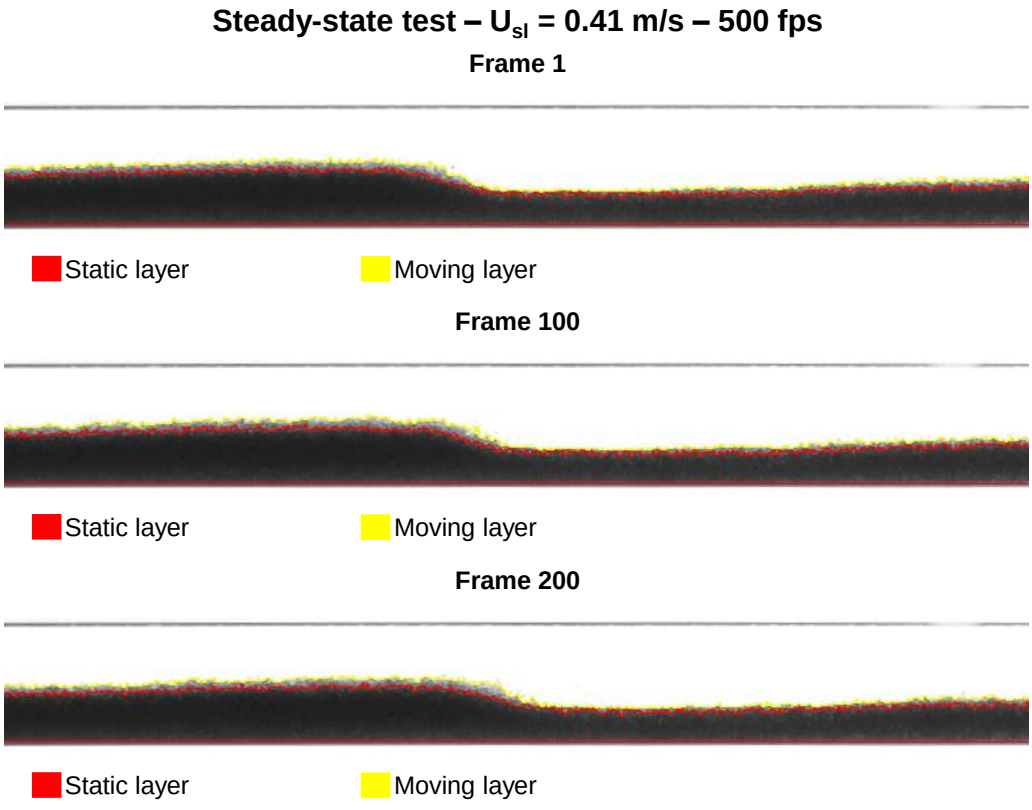

Figure 5.8 A steady-state test at U_{sl} of 0.41 m/s, recorded at a frame rate of 500 fps

Figure 5.9 shows a few selected frames of the steady-state test at U_{sl} of 0.71 *m/s*, recorded at a frame rate of 500 *fps.* At this high U_{sl} the dunes are separated from one another. This steady-state test shows more variation from frame to frame, even though it is recorded at the same frame rate as the previous test, but a higher flow velocity.

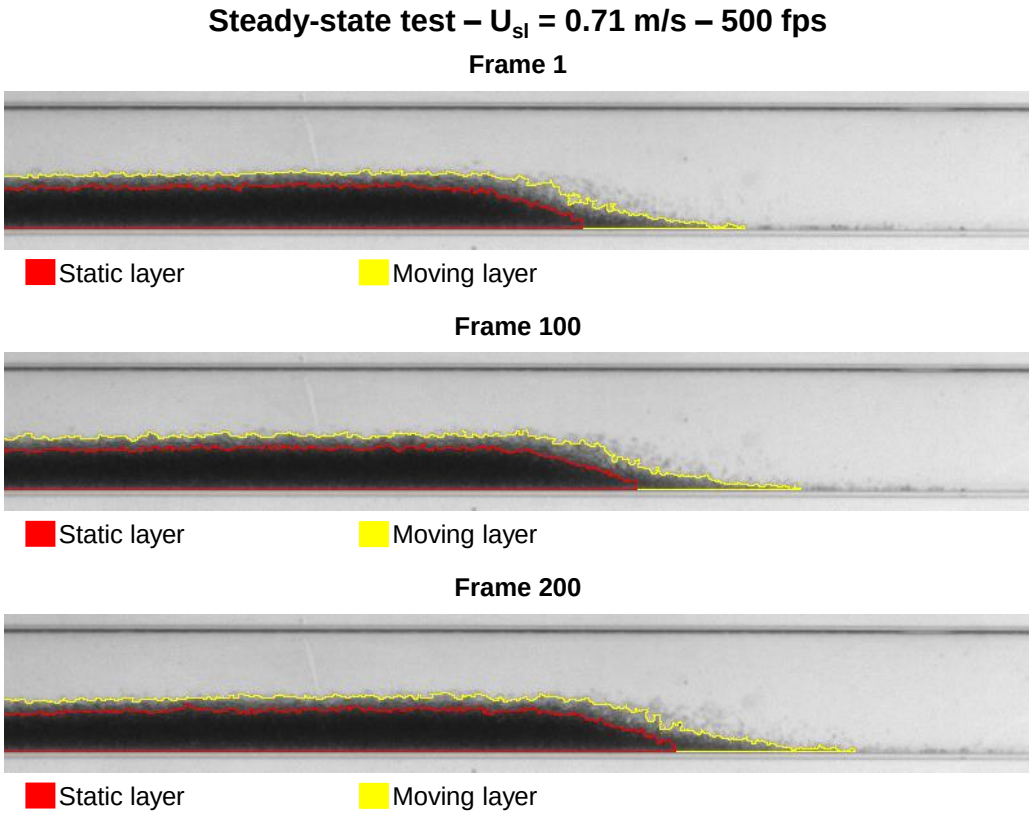

Figure 5.9 A steady-state test at U_{sl} of 0.71 m/s, recorded at a framerate of 500 fps

Figure 5.10 shows a few selected frames of the dynamic test at U_{sl} of 0.47 *m/s*, recorded at a frame rate of 8 *fps*. A single particle dune moves through the HTS. Due to the low frame rate of the recording, the changes between the frames are more noticeable during the dynamic test than the steady state tests. The dynamic test starts recording before the particle dune enters the HTS, and stops after the dune has left the HTS.

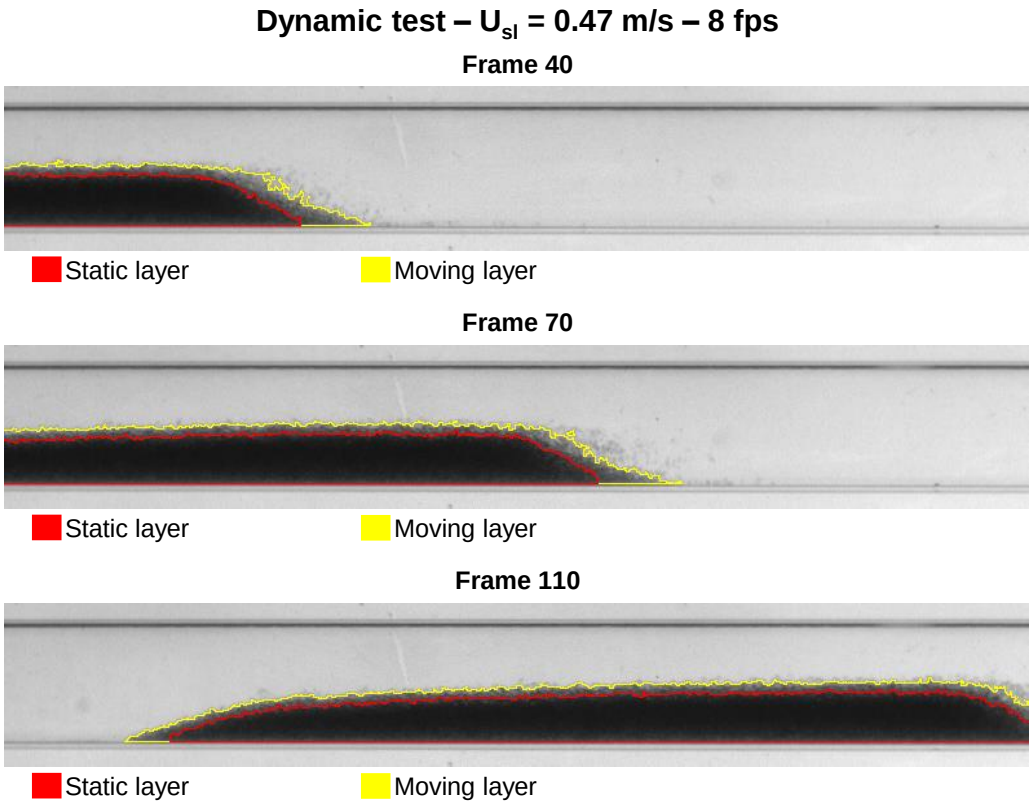

Figure 5.10 The dynamic test at U_{sl} of 0.47 m/s, recorded at a frame rate of 8 fps

5.2.1 Particle concentration

The particle volume concentration is calculated using the particle concentration method described in chapter 4.2.4. The results for liquid-particle flows at two different U_{sl} are shown in Figure 5.11, at U_{sl} of 0.41 *m/s* (a) and 0.71 *m/s* (b). The figures are showing the particle volume concentrations calculated from 200 frames, recorded at a frame rate of 500 *fps*. As a result, the time series are only 0.398 *s* long. At the low U_{sl} (a), the dunes move too slow for any noticeable changes to be recorded. As can be seen from the figure, the concentrations show little variations. The high U_{sl} (b), on the other hand, starts recording right after the front of a dune has entered the HTS. Both the static and the moving layer shows an increase in volume concentration.

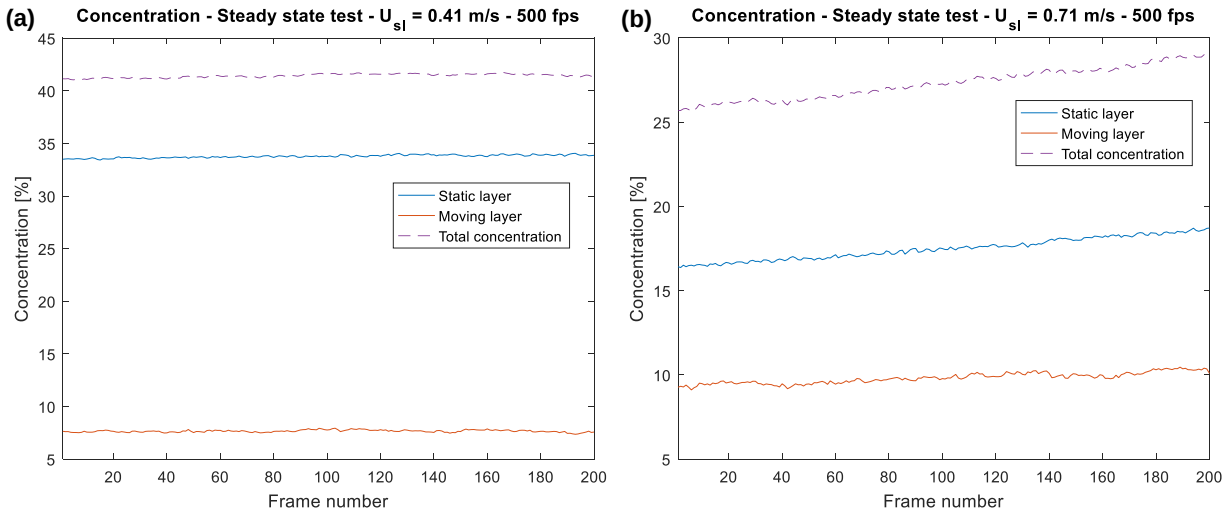

Figure 5.11 Volume concentration of the static and moving layers during steady-state tests at **a)** a U_{sl} of 0.41 m/s and **b)** a U_{sl} of 0.71 m/s

For the dynamic test, where only a limited number of particles were injected, a single particle dune moves through the HTS. The resulting volume concentrations for both layers are shown in Figure 5.12. The flow was recorded at a frame rate of 8 *fps*, and the particle dune was recorded while moving through the entirety of the HTS. The imaging starts with an empty pipe, so naturally the concentration is 0. As the dune moves into the shot, the static and moving layer volume concentrations increases and reaches a maximum at around frame number 100. The dune continues out of the shot, and the volume concentration of both layers gradually returns to 0.

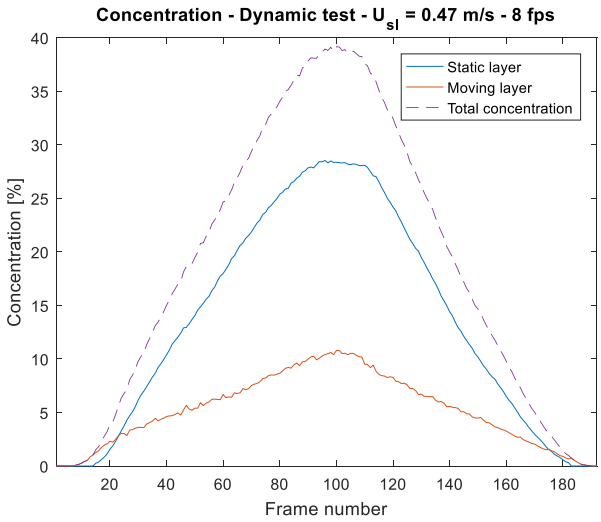

Figure 5.12 Volume concentration of the static and moving layers during the dynamic test

5.2.2 Particle dune velocity

The calculation of the particle dune velocity uses the cross-correlation method described in chapter 4.2.4. Figure 5.13 shows the cross-correlation performed on the image series recorded at a U_{sl} of 0.41 *m/s*. The flow was recorded during steady-state conditions. The two frames used to perform the cross-correlation were frame number 1 and frame number 200 in a series recorded at a frame rate of 500 *fps*, the frames were, therefore, recorded with a time difference of 0.398 *s*. The results of the cross-correlation showed a shift of the dune front of 17.3 *mm* and the resulting dune velocity was 43.4 *mm/s*.

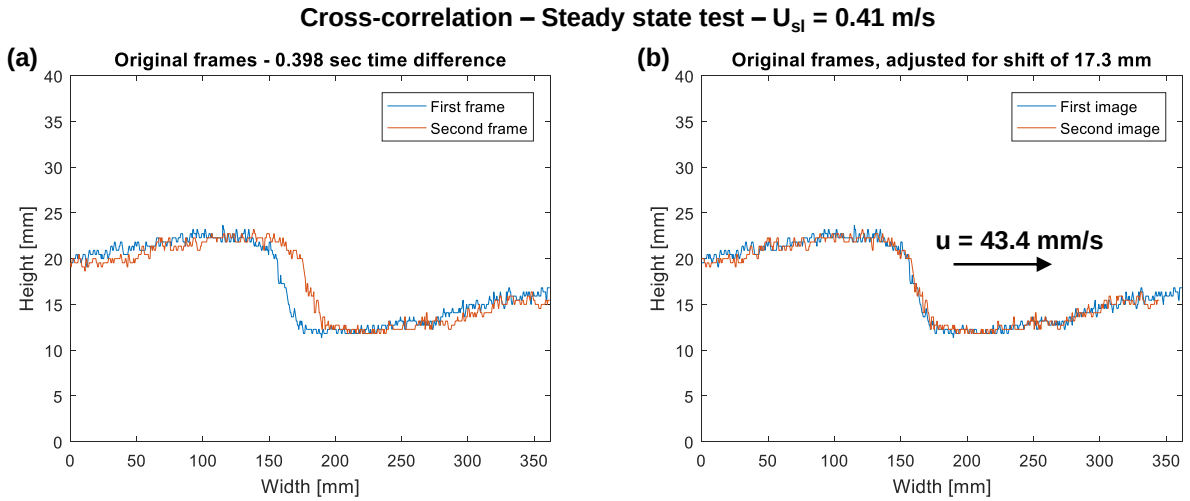

Figure 5.13 Cross-correlation of a steady-state test at U_{sl} of 0.41 m/s **a)** shows the original images and **b)** shows the images adjusted for the calculated shift

Figure 5.14 shows the cross-correlation performed on an image series recorded at a U_{sl} of 0.71 *m/s*. The flow was recorded during steady state-conditions. The two frames used to perform the cross-correlation were frame number 1 and frame number 198 in a series recorded at a frame rate of 500 *fps*, this lead to a 0.396 *s* time difference between the frames. The cross-correlation showed a shift of the dune front of 33.3 *mm* and the resulting dune front velocity was 83.2 *mm/s*.

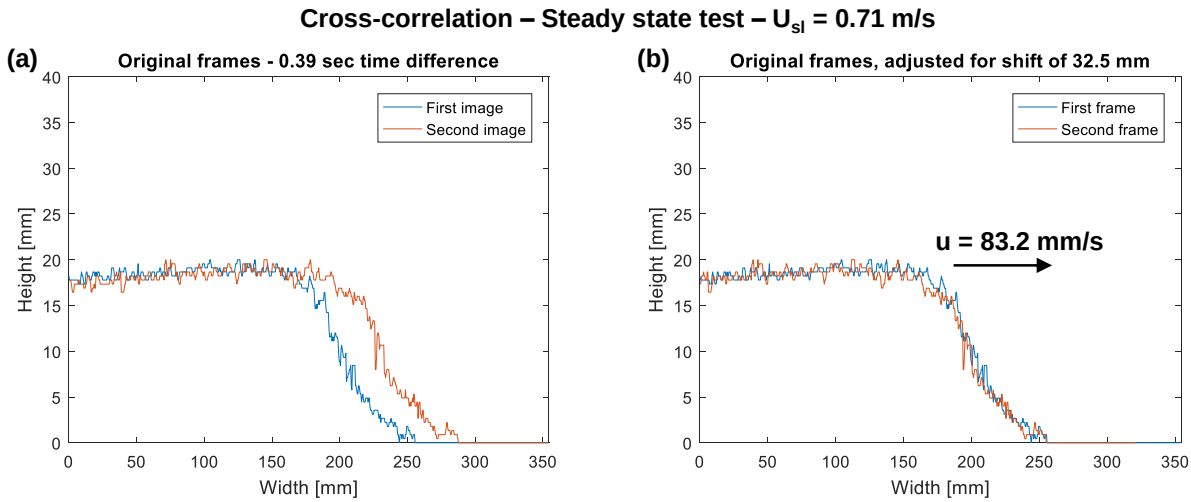

Figure 5.14 Cross-correlation of a steady-state test at U_{sl} of 0.71 m/s **a)** shows the original images and **b)** shows the images adjusted for the calculated shift

Figure 5.15 shows the cross-correlation of an image series recorded at U_{sl} of 0.47 *m/s*. The flow was recorded during dynamic conditions. The frames used for the cross-correlation was frame number 50 and frame number 70 in a series recorded at a frame rate of 8 *fps*, resulting in the frames being recorded 2.5 *s* apart. The cross-correlation showed a shift of the dune front of 68.5 *mm* and the resulting dune front velocity was 27.4 *mm/s*.

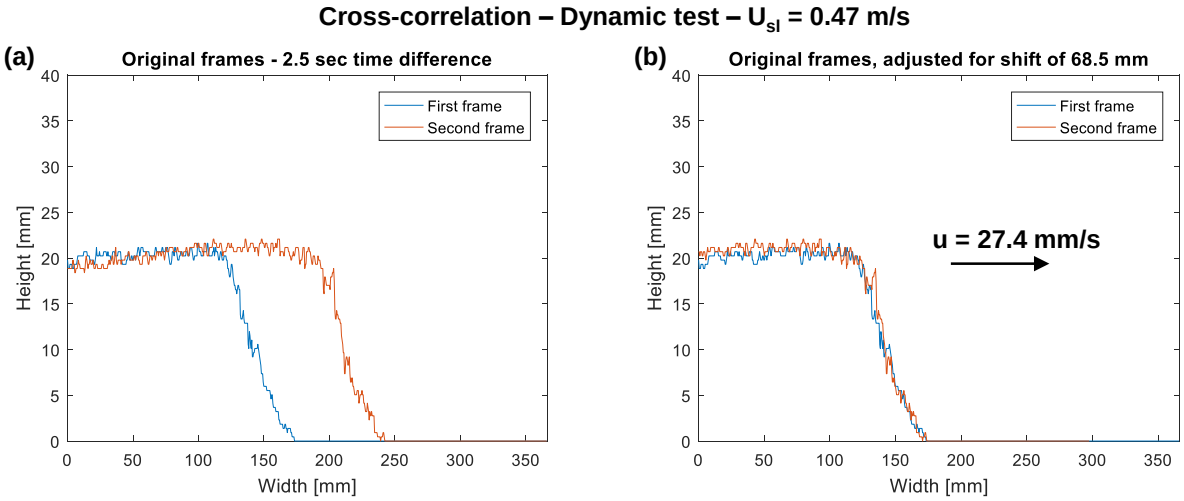

Figure 5.15 Cross-correlation of a dynamic test at U_{sl} of 0.47 m/s **a)** shows the original images and **b)** shows the images adjusted for the calculated shift

The steady-state tests (Figure 5.13 and Figure 5.14) show the result that one would expect. An increase of superficial liquid velocity resulted in an increase in dune front velocity. The superficial velocity of the liquid in Figure 5.14 is 1.73 times higher than in Figure 5.13, whereas the dune front velocity is 1.92 times higher.

For the dynamic test on the other hand (Figure 5.15), the superficial velocity was slightly higher than the lowest velocity of the steady-state test (Figure 5.13), yet the dune front velocity is significantly lower (43.4 *mm/s* for the steady state test and 27.4 *mm/s* for the dynamic test). This is most likely due to the presence of a continuous bed in the steady-state test. This reduced the flow area for the liquid, resulting in higher liquid velocities in the moving layer and consequently a higher dune front velocity.

A dune front velocity of 43.4 *mm/s* means that the dune front takes 35.0 *s* to move the 1520 *mm* from the high side pressure tap, P_H, to the low side pressure tap, P_L. This corresponds to a frequency of 0.0286 *Hz* for the case with a U_{sl} of 0.41 *m/s*. Similarly, a dune front velocity of 83.2 *mm/s* for the case with a U_{sl} of 0.71 *m/s* means the dune takes 18.3 *s* to move the 1520 *mm* between the pressure taps. This corresponds to a frequency of 0.0546 *Hz*. The frequency calculated from the movement of the dunes matches up well with the frequency range obtained from the PSD plots in Figure 5.4 and Figure 5.5. The process of comparing the PSD and image process is illustrated in Figure 5.16. The frequencies obtained from the PSD and the image processing is in agreement with results reported by Takahashi et al. (1989), where low frequency responses in the PSD was attributed to the movement of dunes.

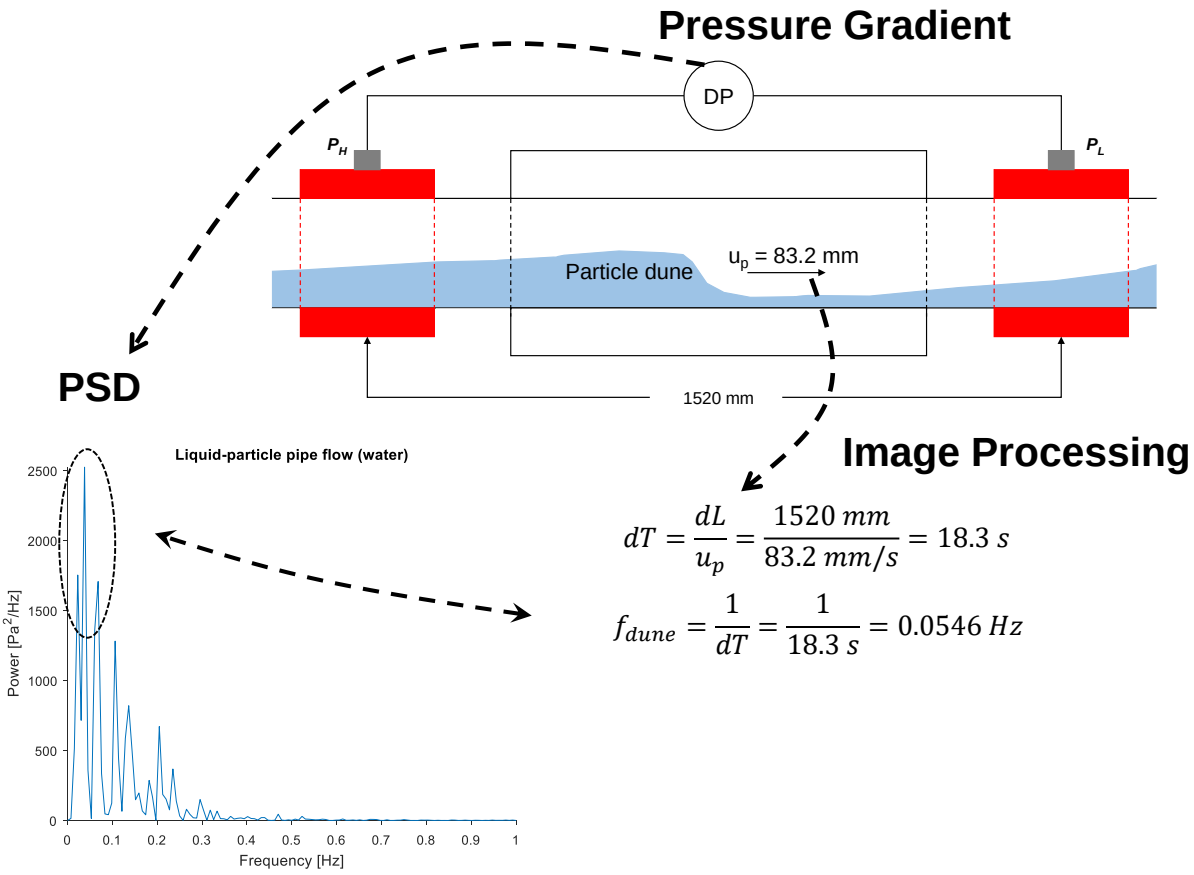

Figure 5.16 Illustration of the comparison between the PSD and the dune velocity from the image processing

5.2.3 Bed height

Figure 5.17 shows the bed height calculated using the method described in chapter 4.2.4. The bed height is calculated for two superficial liquid velocities, a U_{sl} of 0.41 *m/s* (a) and a U_{sl} of 0.71 *m/s* (b) at steady-state conditions. The window width of the window of the investigation was 50 *px*, or approximately 22.7 *mm*, for both cases. The figure shows the height change from the previous frame on the y-axis. The x-axis shows the frame number, starting on frame 2 and continuing to the end of the recorded series, frame number 200 in both cases (For example, a value of 2 on the x-axis shows the height change from frame 1 to frame 2). The window of investigation was selected to be set ahead of the front of the dune in each case, to calculate the height changes as the dune front entered the window of investigation.

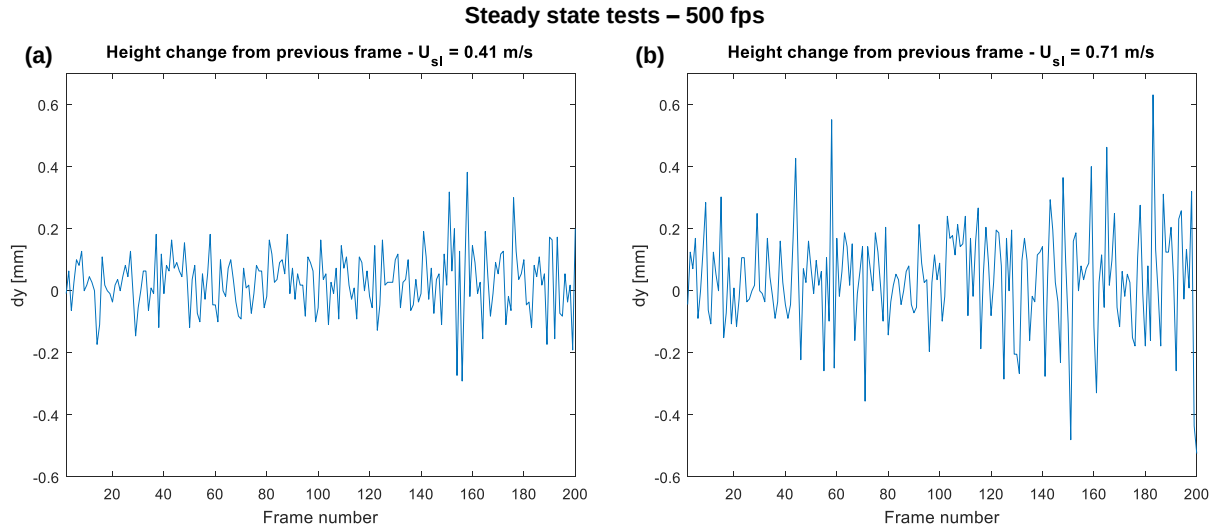

Figure 5.17 Plots of height changes during steady state tests for **a)** U_{sl} of 0.41 m/s and **b)** U_{sl} of 0.71 m/s, both with recording frame rate of 500 fps.

Figure 5.18 shows the bed height calculated using the method described in chapter 4.2.4. The bed height is calculated at a U_{sl} of 0.47 *m/s* at dynamic conditions. The figure shows the height change from the previous frame on the y-axis. The x-axis shows the frame number, starting with frame 2 and continuing to the end of the recorded series, frame number 192 in this case. The window of investigation was 50 *px* wide, and was fixed in the middle of the section recorded by the camera. As can be seen from the figure, the bed height remains at 0 for nearly 50 frames as the dune has

not reached the window of investigation yet. As the wave reaches the window, a height increase can be seen for the following frames. At around frame 75, the maximum height of the dune has entered the window, and thus the height will start to decrease as the dune continues. The following negative values is a result of the dune leaving the window of investigation. At frame 150, the dune has completely left the window of investigation, and the height change remain at 0. The height change can be seen to fluctuate a lot. This is because the particles being transported in the moving layer show signs of saltation. This saltation will cause a momentary height increase, even though the trend is that the height is decreasing.

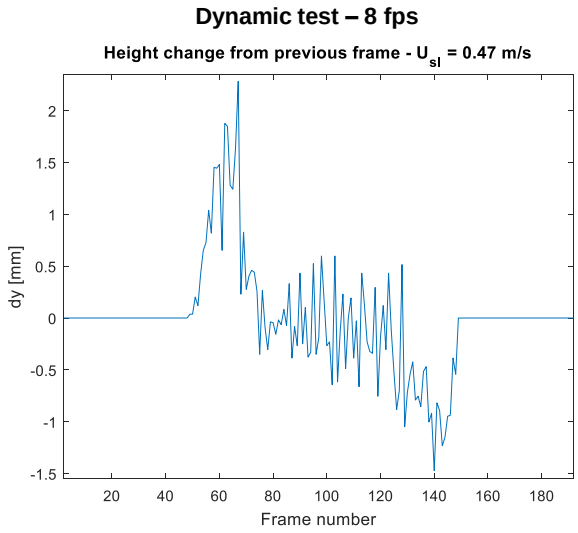

Figure 5.18 Plot of height changes for a dynamic test at U_{sl} of 0.47 m/s

6 Conclusion

Experiments were carried out for single-phase liquid flow and two-phase liquid-particle flow, using a medium-scale flow loop. The liquid was water and the particles were glass pellets. The differential pressure in the horizontal and inclined test sections was measured. The horizontal test section represented flow in a pipe, whereas the inclined section had a drill string inside and represented flow in an annulus. Power spectral density analysis was performed on the recorded time-series pressure gradient data. In addition, images of the liquid-particle flow patterns were recorded using the high-speed camera. An image processing algorithm and a GUI interface were developed for image analysis. The following conclusions were reached:

- The frequency corresponding to the rotating drill string was clearly detected in the frequency spectrum.
- The introduction of particles to a liquid flow caused significant changes to the PSD, where high-amplitude and low-frequency peaks were observed.
- The amplitude response from the particles movements was so high that the amplitude response from the rotating drill string could barely be seen for this particular size of particles.
- The developed algorithm for image processing gave the possibility of calculating the particle concentration, bed height and particle dune velocity from the images.
- Amplitude peaks at a higher frequency corresponding to the particle dune movement indicated better hole cleaning.
- The frequency calculated from the particle dune front velocity matched up well with the frequencies obtained from the PSD analysis.

References

Fast Fourier Transform. (n.d.). Retrieved from https://se.mathworks.com/help/matlab/ref/fft.html

Felipe, C. A. S., & Rocha, S. C. S. (2004). Time series analysis of pressure fluctuation in gas-solid fluidized beds. *Brazilian Journal of Chemical Engineering*, 24(3), 497-507.

He, H., Lu, X., Shuang, W., Wang, Q., Kang, Y., Yan, L., Ji, X., Luo, G., & Liu, H. (2014). Statistical and frequency analysis of the pressure fluctuation in a fluidized bed of non-spherical particles. *Particuology*, 16, 178-186.

Heinzel, G., Rüdiger, A., & Schilling, R. (2002). *Spectrum and spectral density estimation by the discrete Fourier transform (DFT), including a comprehensive list of window functions and some new flat-top windows* [pdf]. Retrieved from https://holometer.fnal.gov/GH_FFT.pdf

Johnsson, F., Zijerveld, R. C., Schouten, J. C., van den Bleek, C.M., & Leckner, B. (2000). Characterization of fluidization regimes by time-series analysis of pressure fluctuations. *International Journal of Multiphase Flow*, 26(4), 663-715.

Kim, Y. J., & Hwang, Y. K. (2003). Experimental sudy on the vortex flow in a concentric annulus with a rotating inner cylinder. *KSME International Journal*, 17(4), 562-572.

McCann, R. C., Quigley, M. S., Zamora, M., & Slater, K. S. (1993). Effects of high-speed rotation on pressures in narrow annuli. *SPE Drilling and Completion*, 10(2), 96-103.

M'chirgui, A., Tadrist, H., & Tadrist, L. (1997). Experimental investigation of the instabilities in a fluidized bed origin of the pressure fluctuations. *Physics of Fluids*, 9(3), 500-509.

Nouri, J. M., & Whitelaw, J. H. (1993). Flow of Newtonian and non-Newtonian fluids in an eccentric annulus with rotation of the inner cylinder. *International Journal of Heat and Fluid Flow*, 18(2), 236-246.

Pahk, J. B., & Klinzing, G. E. (2008a). Comparison of flow characteristics for dilute phase pneumatic conveying for two different plastic pellets. *Journal of the Chinese Institute of Chemical Engineers*. 39(2), 143-150.

Pahk, J. B., & Klinzing, G. E. (2008b). Assessing flow regimes from pressure fluctuations in pneumatic conveying of polymer pellets. *Particulate Science and Technology*, 26(3), 247-256.

Rabenjafimanantosa, A. H., Time, R. W., Saasen, A. (2005). Flow regimes over particle beds: experimental studies of particle transport in horizontal pipes. *Annual Transactions of The Nordic Rheology Society*, 13, 99-106.

Rabenjafimanantosa, A. G., Time, R. W., Hana, M., Saasen, A. (2005). Dunes dynamics and turbulence structures over particle beds – Experimental studies and numerical simulations. *Annual Transactions of The Nordic Rheology Society*, 13, 171-176.

Roberts, S. 2003. *Lecture 7 – The Discrete Fourier Transform* [pdf]. Retrieved from University of Oxford, Signal processing & filter design. Retrieved from http://www.robots.ox.ac.uk

Takahashi, H., Masuyama, T., & Noda, K. (1989). Unstable flow of a solid-liquid mixture in a horizontal pipe. *International Journal of Multiphase Flow*, 15(5), 831-841.

Takahashi, H. (2003, 6-10 July). *Modelling of cutting transport for hole cleaning in horizontal and highly inclined wells by coiled tubing drilling*. Paper presented at the 4th ASME/JSME Joint Fluids Engineering Conference, Honolulu, Hawaii, USA.

Tomren, P. H., Iyoho, A. W., & Azar, J. J. (1986). Experimental study of cuttings transport in directional wells. *SPE Drilling Engineering*, 1(1), 43-56.

Vásquez, N., Jacob, K., Cocco, R., Dhodapkar, S., & Klinzing, G. E. (2008). Visual analysis of particle bouncing and its effect on pressure drop in dilute phase pneumatic conveying. *Powder Technology*, 179(3), 170-175.

Woo, N. S., Kim, Y. J., Kwon. J. K., Chung, S. K., & Park, E. S. (2011, 19-24 June). *A study on the solid-liquid rotating flow for cuttings transportation in inclined annulus*. Paper presented at the 21st International Offshore and Polar Engineering Conference, Maui, Hawaii, USA.

Appendix

Appendix A: Calculating the PSD and plotting the PSD and time-series

```
clear
close all

%% Constant values
d = 40/1000;                % inner pipe diameter [m]
area = (pi/4)*d^2;          % Flow area of inner pipe [m^2]
d2 = 25/1000;               % DS diameter [m]
area2 = (pi/4)*d2^2;        % Area of drill string [m^2]
area3 = area-area2;         % Flow area in drill string section [m^2]
L_H = 1.52;                 % Distance between two pressure taps [m]
L_5 = 1.52;                 % Distance between two pressure taps [m]
L_35 = 0.60;                % Distance between two pressure taps [m]
L_bend = 0.57;              % Distance between two pressure taps [m]

%% Extract data from text file

% Define pressure to be investigated
% 0 = DP0 - horizontal section
% 1 = DP2 - 5 degree section
inv_start = 1;

% Values used to read file
pump_frequency = 8;     % Frequency of the wall mounted inverter
ds_rotation = 100;      % Rotation of the drill string

% Read file and extract raw data
formatSpec = '%d';
sizeA = [1 1];
fileinv = ['f' num2str(pump_frequency) 'rpm' num2str(ds_rotation) '.txt'];
fileID = fopen(fileinv);
fs = fscanf(fileID,formatSpec,sizeA);   % Extracting sampling frequency ...
% from the text file
fclose(fileID);
A = dlmread(fileinv,'\t',1,0); % Reading the data from the file, starting on
row 2

f_end = 3; % Frequency the x-axis of the PSD plot will end at

% Extracting differential pressures, flow rate, and temperature
DP0 = A(:,1)*100;       % Pressure gradient signal DP0 - horizontal [Pa]
DP0_avg = mean(DP0);    % Average of horizontal signal [Pa]
DP1 = A(:,2);           % Pressure differential signal DP1 - 35 degree [Pa]
DP2 = A(:,3)*100;       % Pressure differential signal DP2 - 5 degree [Pa]
DP2_avg = mean(DP2);    % Average of 5 degree signal [Pa]
DP3 = A(:,4);           % Pressure differential signal DP3 - bend [Pa]
Rate = A(:,5)/3600;     % Mass flow rate signal [kg/s]
Rate_avg=mean(Rate);    % Average of flow rate signal [kg/s]
```

```
Temp = A(:,6);          % Temperature signal [C]
Temp_avg = mean(Temp);  % Average temperature of entire signal [C]
Temp_avg = round(Temp_avg*100)/100; % Temperature rounded to two decimals  [C]
N=length(DP2);          % Length of signal (amount of data points)
Usl = 0.0605*pump_frequency-0.0111; % Flow velocity without drill string [m/s]
Usl_5 = Usl*area/area3; % Flow velocity in inclined section [m/s]
Usl = round(Usl*100)/100; % Usl rounded to two decimals
Usl_5 = round(Usl_5*100)/100; % Usl_5 rounded to two decmials

%% Choose interval of investigation
% t_start = 0;          Standard start value to evaluate whole file
% t_end = (N-1)/fs;     Standard end value to evaluate whole file
t_start = 0;                % Time interval to start investigation
t_end = (N-1)/fs;           % Time interval to end investigation

N_t_start = t_start*fs+1;   % Vector position of start of investigation ...
% interval
N_t_end = t_end*fs+1;       % Vector position of end of investigation ...
% interval
n_v = (N_t_start:N_t_end);
n = length(n_v);

t = 0:1/fs:(N-1)/fs;     % Time vector of signal
T = 0:1/fs:(n-1)/fs;

%% Performing FFT and plotting

if inv_start == 0
    inv = DP0;
else
    inv = DP2;
end
DP=inv-mean(inv); % Removing average from chosen pressure differetianl.
fig_time = figure('Name','Time Domain Plot','NumberTitle','off');
DP_fft = inv(N_t_start:N_t_end); % Limiting FFT to the chosen time interval
plot(T,DP_fft,'Color',[0,0.447,0.741]) % Time domain plot of the file ...
% in the chosen interval
if inv_start == 0
    plot(T,DP_fft/L_H,'Color',[0,0.447,0.741]) % Time domain plot of ...
% the pressure gradient in the horizontal section
    title_psd = ['Liquid pipe flow (water)'];
    title(title_psd)
else
    plot(T,DP_fft/L_5,'Color',[0,0.447,0.741]) % Time domain plot of ...
% the pressure gradient in the inclined section
    title_psd = ['Liquid-particle annular flow (water), \omega = ' ...
        num2str(ds_rotation) ' RPM'];
    title(title_psd)
end
ylabel('dP/dL [Pa/m]')
xlabel('Time [s]')
axis([0 T(end) -inf inf])
set(gca,'TickDir','out')

fig_freq = figure('Name','Frequency Domain Plot','NumberTitle','off');
DP_fft_avg = mean(DP_fft);
```

```
DP = (DP_fft-DP_fft_avg);


% Performing the Power Spectral Density
xdft = fft(DP);
if mod(n,2)
   xdft = xdft(1:(n+1)/2);
else
    xdft = xdft(1:(n)/2+1);
end
psdx = abs(xdft/n).^2;
psdx(2:end-1) = 2*psdx(2:end-1);
freq = 0:fs/n:fs/2;     % Frequency values for plotting the PSD

% Plotting the Power Spectrum
plot(freq,psdx,'Color',[0,0.447,0.741]) % Plot of the PSD
xlabel('Frequency [Hz]')
ylabel('Power [Pa^2/Hz]')
if inv_start == 0
    title_psd = ['Liquid pipe flow (water)'];
    title(title_psd)
else
    title_psd = ['Liquid-particle annular flow (water), \omega = ' ...
        num2str(ds_rotation) ' RPM'];
    title(title_psd)
end
axis([0 f_end 0 inf]);
set(gca,'TickDir','out')
box off

% Save location for the plots
directory = 'C:\Users\Reinert\SkyDrive\Master thesis\PSD Plots\';

% If loop to save the plots
if inv_start == 0
    name_time = [directory 'Usl' num2str(Usl) 'timedomain' ...
        num2str(rpm) 'rpm.emf'];
    name_freq = [directory 'Usl' num2str(Usl) 'frequencydomain' ...
        num2str(rpm) 'rpm.emf'];
    saveas(fig_time,name_time);
    saveas(fig_freq,name_freq);
else
    name_time = [directory 'L-P-Usl_a' num2str(Usl_5) ...
        'timedomain' num2str(ds_rotation) 'rpm.emf'];
    name_freq = [directory 'L-P-Usl_a' num2str(Usl_5) ...
        'frequencydomain' num2str(ds_rotation) 'rpm.emf'];
    saveas(fig_time,name_time);
    saveas(fig_freq,name_freq);
end
```